

On the symmetry-breaking instability of the flow past axisymmetric bluff bodies

Alessandro Chiarini^{1,2}, Romain Gauthier³ and Edouard Boujo³

Corresponding authors: Alessandro Chiarini, alessandro.chiarini@polimi.it; Edouard Boujo, edouard.boujo@epfl.ch

(Received 6 November 2024; revised 5 April 2025; accepted 19 June 2025)

The primary bifurcation of the flow past three-dimensional axisymmetric bodies is investigated. We show that the azimuthal vorticity generated at the body surface is at the root of the instability, and that the mechanism proposed by Magnaudet & Mougin (2007, *J. Fluid Mech.*, vol. 572, 311–337) in the context of spheroidal bubbles extends to axisymmetric bodies with a no-slip surface. The instability arises in a thin region of the flow in the near wake, and is associated with the occurrence of strong vorticity gradients. We propose a simple yet effective scaling law for the prediction of the instability, based on a measure of the near-wake vorticity and of the radial extent of the separation bubble. At criticality, the resulting Reynolds number collapses approximately to a constant value for bodies with different geometries and aspect ratios, with a relative variation that is one order of magnitude smaller than that of the standard Reynolds number based on the free-stream velocity and body diameter. The new scaling can be useful to assess whether the steady flow past axisymmetric bodies is globally unstable, without the need for an additional stability analysis.

Key words: wakes, instability

1. Introduction

1.1. Axisymmetric three-dimensional bluff bodies

The flow past a stationary isolated axisymmetric body may be considered as a simplified case of a more general family of immersed three-dimensional (3-D) bluff bodies, which

© The Author(s), 2025. Published by Cambridge University Press. This is an Open Access article, distributed under the terms of the Creative Commons Attribution licence (https://creativecommons.org/licenses/by/4.0/), which permits unrestricted re-use, distribution and reproduction, provided the original article is properly cited.

¹Complex Fluids and Flows Unit, Okinawa Institute of Science and Technology Graduate University, 1919-1, Tancha, Onna-son, Okinawa 904-0495, Japan

²Dipartimento di Scienze e Tecnologie Aerospaziali, Politecnico di Milano, via La Masa 34, 20156 Milano, Italy

³Laboratory of Fluid Mechanics and Instabilities, École Polytechnique Fédérale de Lausanne, CH-1015 Lausanne, Switzerland

are ubiquitous in human life and engineering applications. In spite of the symmetries of the body, instabilities are known to generate asymmetric and possibly unsteady flows; different regimes are indeed possible depending on the Reynolds number $Re = U_{\infty}H/\nu$, based on the body cross-stream dimension H, the free-stream velocity U_{∞} and the fluid kinematic viscosity ν . In this work, we focus on the primary symmetry-breaking instability.

The flow past 3-D axisymmetric bodies becomes asymmetric before transitioning to an unsteady regime (Magarvey & Bishop 1961a,b; Magarvey & MacLatchy 1965). The steady axisymmetric flow past a sphere, for example, is known to transition to a steady asymmetric state at $Re \approx 211$ (Johnson & Patel 1999) through the regular bifurcation of an eigenmode of azimuthal wavenumber m = 1 (Tomboulides & Orszag 2000). This bifurcation gives origin to a pair of counter-rotating steady streamwise vortices in the wake, which are not aligned with the flow but possess a reflectional symmetry about a longitudinal plane of arbitrary azimuthal orientation, and exhibit an eccentricity that increases with the distance from the body. The same bifurcation has been observed for the flow past other axisymmetric bodies, e.g. disks and bullet-shaped bodies (slender cylindrical bodies with a smooth leading edge and a blunt trailing edge). The flow past a disk placed perpendicular to the incoming flow exhibits the primary regular bifurcation towards an asymmetric state at Reynolds number $Re \approx 115$ (Natarajan & Acrivos 1993; Fabre, Auguste & Magnaudet 2008; Meliga, Chomaz & Sipp 2009a). The flow past a bullet-shaped body undergoes the same bifurcation, but at a larger Reynolds number (Brucker 2001; Bohorquez et al. 2011) that increases with the length-to-diameter aspect ratio $\mathcal{R} = L/H$ of the body, e.g. $Re \approx 216$ for $\mathcal{R} = 1$, and $Re \approx 435$ for $\mathcal{R} = 6$. A similar dependence on \mathcal{R} has been observed by Chrust, Bouchet & Dusek (2010) for the flow past flat cylinders whose axis is parallel to the free stream. They observed that the flow bifurcates towards an asymmetric state at $Re \approx 115-120$ for $\mathcal{R} \to 0$, and at $Re \approx 270$ for $\mathcal{R}=1.$

The instability mechanism of the primary bifurcation of the flow past axisymmetric bodies has been investigated extensively over the years. Monkewitz (1988) investigated the linear stability of an analytic two-parameter family of axisymmetric, parallel and incompressible wake profiles. He observed that the first helical mode with m=1 displays the largest growth rate for all cases, and that it is the only mode to become absolutely unstable for velocity profiles approximating those found in the near wake. Pier (2008) studied the local absolute instability features of the flow past a sphere, with the aim of linking the local flow properties with the fundamental mechanism driving the global flow bifurcation. He neglected the strong non-parallelism of the near-wake region, and highlighted the local properties by freezing the flow at different streamwise coordinates, and studying the equivalent axially parallel shear flows. In doing so, he demonstrated the existence of absolutely unstable regions in the near wake, and found that the strength and spatial extent of these regions increase with the Reynolds number. The results of Monkewitz (1988) and Pier (2008) clearly hint at the existence of a wavemaker in the wake (an absolutely unstable region where the fluctuations self-sustain), which feeds the convectively unstable region downstream. However, these results cannot fully explain the symmetry breaking corresponding to the first bifurcation of the flow.

1.2. The Magnaudet and Mougin model for free-slip bodies

In the context of free-slip oblate spheroidal bodies, Magnaudet & Mougin (2007) (hereafter referred to as MM) proposed an instability mechanism that accounts for the strongly non-parallel nature of the flow. The theoretical arguments that they put forward are based on the idea that the regular bifurcation of the flow is driven by the azimuthal vorticity $\omega_{\theta} = \partial u_r/\partial z - \partial u_z/\partial r$ generated at the body surface and then transported into

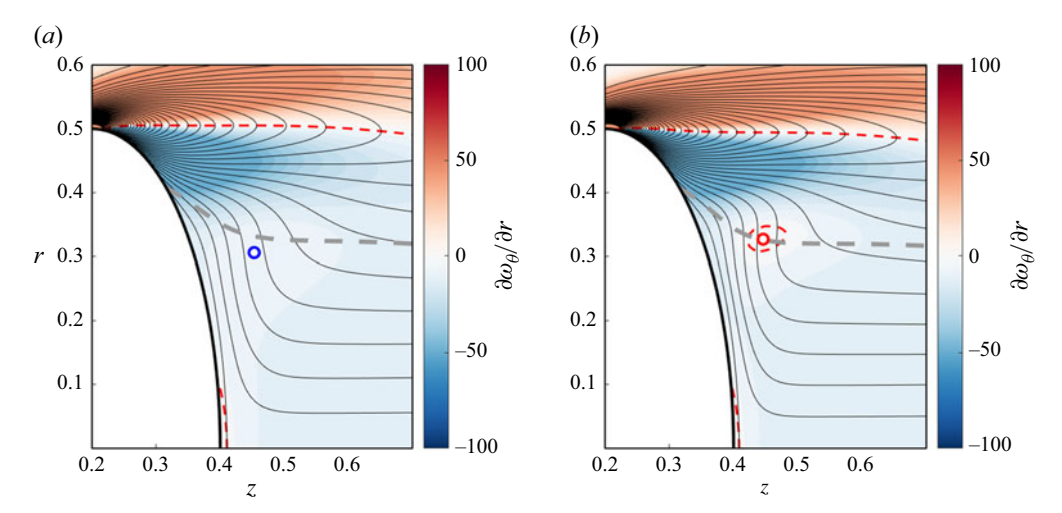


Figure 1. Near-wake distribution of the azimuthal vorticity around an ellipsoid with free-slip surface and $\Re = 0.4$ for (a) Re = 200 and (b) Re = 270. Black lines are isocontours of the azimuthal vorticity ω_{θ} , and coloured contours show $\partial \omega_{\theta}/\partial r$. The grey dashed line shows $u_z = 0$, and the red dashed line shows $\partial \omega_{\theta}/\partial r = 0$. Blue/red circles indicate the negative/positive maxima of $\partial \omega_{\theta}/\partial r$ in the near-wake region.

the wake (where (u_r, u_z) are the velocity components in the radial and axial directions r and z). For free-slip ellipsoids, in fact, they found that the wider range of Re for which the flow becomes unstable as R increases (see figure 7 of their paper) well correlates with the increase in maximum surface vorticity $\omega_{\theta,max}$ and normal diffusive vorticity flux at the body surface (see § 3 of their paper). They suggested that the instability originates in a thin region of the flow downstream the body. By inspecting the vorticity field, they observed that two distinct regions may be identified (see figure 21 of their paper and figure 1): (i) very close to the body, isocontours of ω_{θ} are almost parallel to the free-slip surface; (ii) farther downstream in the wake recirculation region, instead, isocontours of ω_{θ} are almost parallel to the symmetry axis, because of the tendency of ω_{θ}/r to approach a constant value as Re increases. At large Reynolds numbers, indeed, the spatial distribution of the vorticity in the recirculation region of the steady viscous flow past an axisymmetric body resembles that of a Hill spherical vortex (Hill 1894; Batchelor 1967); see e.g. figure 10 in Fornberg (1988) and the related discussion. Thus MM conjectured that the instability arises in the transition region where isocontours of ω_{θ} have to turn to satisfy the conditions both at the body surface and in the wake recirculation region. As Re increases, this transition region shrinks, and isocontours of ω_{θ} must turn more and more sharply, resulting in stronger and stronger vorticity gradients.

In an attempt to provide a rational instability criterion, MM related the flow bifurcation to the appearance of points where $\partial \omega_{\theta}/\partial r=0$ in the near wake. This comes directly from the balance equation for the steady axisymmetric base-flow vorticity, which in cylindrical coordinates reads

$$\underbrace{u_r \frac{\partial \omega_\theta}{\partial r}}_{\text{II}} \underbrace{-u_r \frac{\omega_\theta}{r}}_{\text{II}} + \underbrace{u_z \frac{\partial \omega_\theta}{\partial z}}_{\text{III}} = \underbrace{\frac{1}{Re} \frac{\partial}{\partial r} \left(\frac{1}{r} \frac{\partial (r\omega_\theta)}{\partial r}\right)}_{\text{IV}} + \underbrace{\frac{1}{Re} \frac{\partial^2 \omega_\theta}{\partial z^2}}_{\text{V}}.$$
 (1.1)

We focus on the near-wake region where $\omega_{\theta} < 0$, $u_z < 0$ and $u_r > 0$ (see figure 1). Here, terms II and III on the left-hand side are positive everywhere. As long as ω_{θ} becomes more negative with r (i.e. $\partial \omega_{\theta} / \partial r < 0$), term I on the left-hand side is negative and may,

at least partially, balance terms II and III. When instead an isocontour of ω_{θ} becomes perpendicular to the symmetry axis (i.e. $\partial \omega_{\theta}/\partial r = 0$), term I vanishes and the positive left-hand side can only be balanced by the positive viscous terms IV and V. Note that where $\partial \omega_{\theta}/\partial r = 0$, term IV reduces to $-\omega_{\theta}/(r^2Re) \sim Re^{-1}$. Therefore, as the Reynolds number increases, term V is observed to dominate term IV, and the balance equation reduces to

$$-u_r \frac{\omega_\theta}{r} + u_z \frac{\partial \omega_\theta}{\partial z} \sim \frac{1}{Re} \frac{\partial^2 \omega_\theta}{\partial z^2}.$$
 (1.2)

This implies that to balance the left-hand side, the streamwise gradient of ω_{θ} in term V on the right-hand side has to vary more and more sharply (over a shorter distance along z) as Re increases. The MM idea is that this tendency of the vorticity to become discontinuous in the points where $\partial \omega_{\theta}/\partial r = 0$ underlies the instability mechanism.

Notably, the numerical simulations of MM corroborate their arguments, showing a good correlation between the first appearance of points with $\partial \omega_{\theta}/\partial r = 0$ and the onset of the bifurcation in the context of free-slip axisymmetric bluff bodies. However, despite some hints provided by the same authors (see the concluding discussion in their paper), it is not clear whether axisymmetric bodies with free-slip and no-slip surfaces share this same instability mechanism driven by the vorticity generated at the surface. It is well known, indeed, that the mechanism of vorticity generation on a surface changes with the boundary condition; see the seminal works of Truesdell (1954), Lighthill (1963), Morton (1984), Leal (1989), Wu & Wu (1993), Wu (1995) and Lundgren & Koumoutsakos (1999), and the more recent works of Brøns et al. (2014) and Terrington, Hourigan & Thompson (2020). For no-slip surfaces, the normal diffusion vorticity flux depends on the tangential shear stress and on the pressure gradient, and it is non-null also in the limit case of a flat wall (Wu & Wu 1993). On a free-slip surface, instead, the vorticity appears as a consequence of the continuity of the tangent stresses, and is non-null only in the case of curved surfaces (Wu 1995). Thus the generality of the MM mechanism and the influence of the different vorticity generation mechanisms at no-slip and free-slip surfaces on the primary flow bifurcation are still open questions that deserve further investigation.

1.3. Focus of the present work

To address these questions, we study the flow past no-slip axisymmetric bluff bodies with different shapes and aspect ratios, and focus on the primary symmetry-breaking bifurcation. We consider four geometries – ellipsoids, bullets, cones and bicones – that feature different combinations of smooth/sharp leading edge and smooth/blunt trailing edge (see figure 2). The aspect ratio of the ellipsoid and the bicone is varied over $1 \le \Re \le 5$, and that of the bullet and the cone over $1 \le \Re \le 8$.

We give evidence that the MM instability mechanism captures rather well the primary instability of the flow past axisymmetric bodies with different shapes and surface types. Indeed, we find that the onset of the bifurcation correlates well with the first appearance of points where $\partial \omega_{\theta}/\partial r=0$ in the near wake, not only for free-slip surfaces but also for no-slip surfaces, despite the different vorticity generation mechanism at the surface. As first hinted by MM, this shows that although the vorticity is at the root of the instability, the way it is produced at the wall does not play a major role. We then propose a simple yet effective scaling law that may be used to predict the onset of the instability without the need for an additional stability analysis. Indeed, the large variability of the critical Reynolds number with the geometry (e.g. as mentioned above, $Re_c \approx 115$ for the disk, $Re_c \approx 211$ for the sphere, and $126 \leqslant Re_c \leqslant 435$ for bullet-shaped bodies with $1 \leqslant R \leqslant 6$) clearly shows that the free-stream velocity U_{∞} and the cross-stream dimension H of the

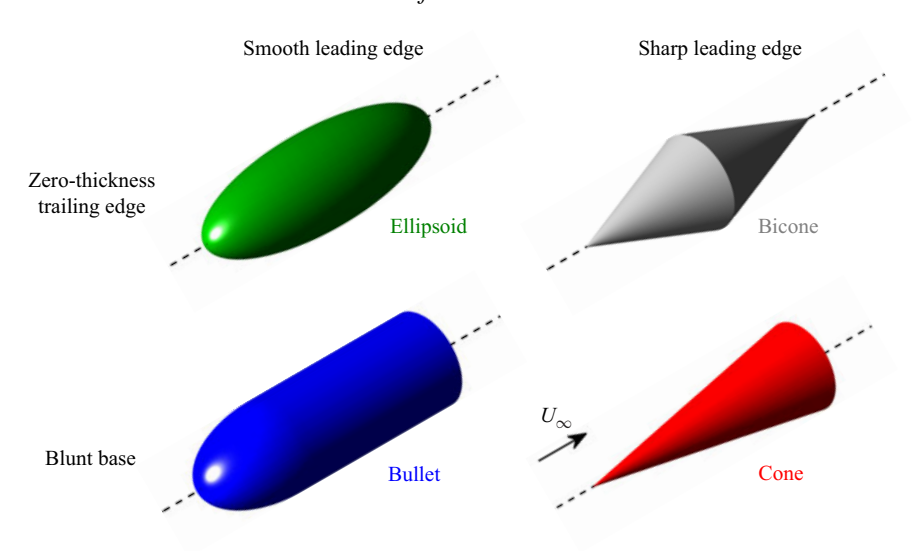


Figure 2. Sketch of the considered geometries. Here, $\mathcal{R} = 3$.

body are not the appropriate velocity and length scales for describing this bifurcation. In the same spirit as Chiarini, Quadrio & Auteri (2022) in the context of two-dimensional (2-D) symmetric bodies, the new scaling is based on quantities related to the physics of the problem, i.e. measures of the vorticity at the body surface and of the radial extent of the wake recirculation region. We show that the resulting Reynolds number, when evaluated at the onset of the bifurcation, collapses rather well to a constant value for all the considered bodies, and thus provides a simple criterion to assess the flow stability.

2. Methods

2.1. Problem formulation

We investigate the primary symmetry-breaking bifurcation of the incompressible flow past 3-D axisymmetric bluff bodies with different geometries and aspect ratios. The bodies have length L and maximum diameter H, and are placed in a uniform flow with velocity U_{∞} aligned with their symmetry axis (see figure 2). Standard cylindrical coordinates are used (with r, θ and z as the radial, azimuthal and axial directions), and the origin is placed at the leading edge of the bodies. The flow is governed by the incompressible Navier–Stokes (NS) equations for the velocity and pressure fields $\{u, p\}$:

$$\frac{\partial \mathbf{u}}{\partial t} + \mathbf{u} \cdot \nabla \mathbf{u} = -\nabla p + \frac{1}{Re} \nabla^2 \mathbf{u}, \quad \nabla \cdot \mathbf{u} = 0, \tag{2.1}$$

with $Re = U_{\infty}H/\nu$. Unless otherwise stated, all quantities are made dimensionless using U_{∞} and H.

We consider four different geometries that yield a base flow with distinct features: ellipsoids, bullets, cones and bicones (see figure 2). The aspect ratio of the bodies $\mathcal{R} = L/H$ is varied over $1 \le \mathcal{R} \le 5$ for ellipsoids and bicones, and over $1 \le \mathcal{R} \le 8$ for bullets and cones. Ellipsoids and bullets possess a smooth leading edge, where the flow separation is driven by the adverse pressure gradient and the position of the separation point changes with the Reynolds number; conversely, cones and bicones feature a zero-thickness sharp leading edge. Bullets and cones have a blunt trailing edge (TE), where

the separation point is enforced by the geometry, and the cross-stream size of the wake recirculation region does not depend on Re and \mathcal{R} ; by contrast, ellipsoids and bicones have a zero-thickness TE, where the flow separation is not set by the geometry, and the size of the wake recirculation region varies with Re and \mathcal{R} .

2.2. Linear stability

The onset of the primary instability is studied using linear theory (Theofilis 2003, 2011). The field $\{u, p\}$ of velocity and pressure is divided into a time-independent axisymmetric base flow $\{u_0, p_0\}$ and an unsteady perturbation $\{u_1, p_1\}$ of small amplitude $0 < \epsilon \ll 1$:

$$u(x, t) = u_0(x) + \epsilon u_1(x, t)$$
 and $p(x, t) = p_0(x) + \epsilon p_1(x, t)$. (2.2)

Introducing this decomposition in the NS equations, one obtains at order ϵ^0 the steady nonlinear NS equations for the base flow $\{u_0, p_0\}$. At order ϵ^1 , one obtains the linearised NS equations for the perturbation field $\{u_1, p_1\}$. By using a normal mode ansatz and a Fourier transform in the azimuthal direction, for each mode the perturbation field takes the form

$$\{u_1, p_1\}(x, t) = \{\hat{u}_1, \hat{p}_1\}(r, z) e^{\lambda t + im\theta} + \text{c.c.},$$
 (2.3)

where m is the azimuthal wavenumber, and c.c. designates the complex conjugate terms. Introducing this expansion in the linearised NS equations yields, for each m, an eigenvalue problem for the complex eigenvalue $\lambda = \lambda_r + i\lambda_i$ and the complex eigenvector $\{\hat{u}_1, \hat{p}_1\}$:

$$\lambda \hat{\boldsymbol{u}}_1 + \mathcal{L}_m \{\boldsymbol{u}_0, Re\} \, \hat{\boldsymbol{u}}_1 + \nabla_m \, \hat{\boldsymbol{p}}_1 = \boldsymbol{0}, \quad \nabla_m \cdot \hat{\boldsymbol{u}}_1 = 0. \tag{2.4}$$

Here, ∇_m is the gradient operator relative to the azimuthal wavenumber m, and \mathcal{L}_m stands for the Fourier-transformed linearised NS operator

$$\mathcal{L}_{m}\{\boldsymbol{u}_{0}, Re\} \,\hat{\boldsymbol{u}}_{1} = \mathcal{C}_{m}(\hat{\boldsymbol{u}}_{1}, \boldsymbol{u}_{0}) - \frac{1}{Re} \nabla_{m}^{2} \hat{\boldsymbol{u}}_{1}, \tag{2.5}$$

where

$$C_m(\boldsymbol{u}_A, \boldsymbol{u}_B) = \boldsymbol{u}_A \cdot \nabla_m \boldsymbol{u}_B + \boldsymbol{u}_B \cdot \nabla_m \boldsymbol{u}_A. \tag{2.6}$$

The flow stability is ascertained by the solution of the generalised eigenvalue problem (2.4) for the complex frequency λ . When $\lambda_r < 0$, the flow is linearly stable, while when $\lambda_r > 0$, the associated global mode is linearly unstable and grows exponentially in time. When $\lambda_i \neq 0$, the unstable mode is time-dependent. When $m \neq 0$, the unstable mode is modulated in the azimuthal direction. Since the focus of the present work is on the primary symmetry-breaking regular bifurcation of the flow past axisymmetric bodies, we restrict our analysis to m = 1.

2.3. Numerical method

The analysis is based on finite elements, and the simulations have been carried out using the COMSOL Multiphysics software (Multiphysics 1998).

Given the axisymmetric nature of the bodies, we consider only the (r, z) plane, and build the mesh in the numerical domain $\{r, z \mid 0 \le r \le 50; -50 \le z \le 150\}$, with nodes strongly clustered near the body. We employ a quadrilateral mesh with eight layers and growth factor 1.2 in the vicinity of the body, and a triangular mesh in the remaining part of the domain. Several sub-domains are used to control the mesh size. The element size decreases from 1 in the far field to 1/120 on the body surface; at the corners, the element size is approximately 10^{-5} . The number of elements changes with the geometry and the

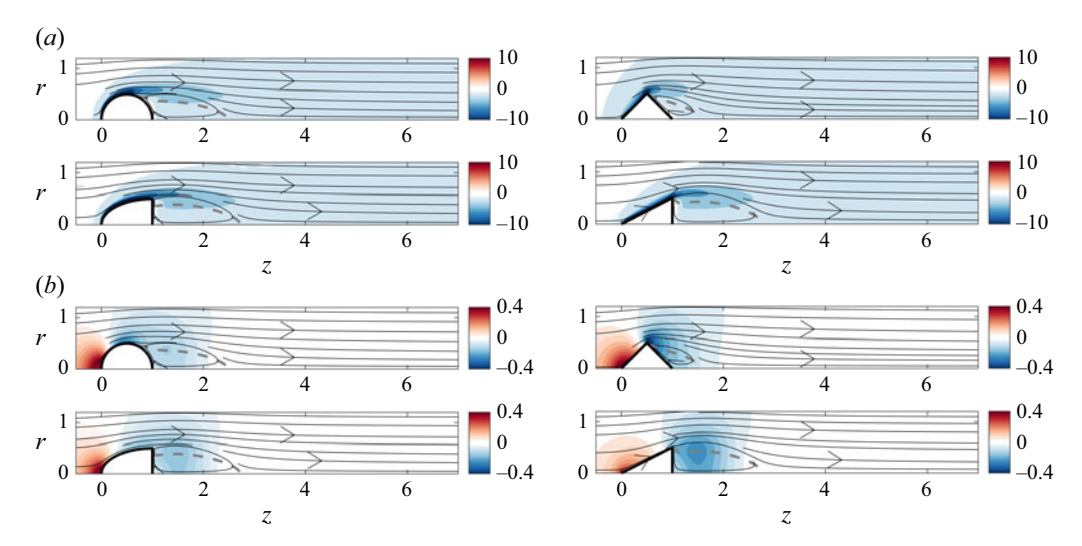


Figure 3. Base flow for $\mathcal{R}=1$ at $Re \approx Re_c$: streamlines and contours of (a) azimuthal vorticity, (b) pressure. Ellipsoid, Re=210; bicone, Re=135; bullet, Re=220; cone, Re=160. Dashed line: $u_{0z}=0$.

aspect ratio. For the shortest and longest bodies, the numbers of elements are 79×10^3 and 126×10^3 for ellipsoids, 83×10^3 and 146×10^3 for bicones, 74×10^3 and 122×10^3 for bullets, and 77×10^3 and 143×10^3 for cones. See Appendix B for details about the mesh convergence.

The low-Re steady axisymmetric base flow $\{u_0, p_0\}$ is obtained by solving the axisymmetric steady version of the NS equations (2.1) using the Newton's iteration method. The NS equations are completed with the following boundary conditions: uniform velocity field $u_0 = U_{\infty}e_z$ at the inlet, stress-free $p_0n - Re^{-1} \nabla u_0 \cdot n = 0$ at the outlet and far field (where n is the unit normal vector), no-slip and no-penetration $u_0 = 0$ on the body surface, and axisymmetry conditions $u_{0r} = \partial_r u_{0z} = \partial_r p_0 = 0$ on the axis r = 0. The generalised eigenvalue problem (2.4) for the onset of the primary instability is then solved using the Arnoldi algorithm, with standard boundary conditions: $u_1 = 0$ at the inlet and on the body surface, stress-free $p_1n - Re^{-1} \nabla u_1 \cdot n = 0$ at the outlet and far field, and m = 1 conditions $\partial_r u_{1r} = \partial_r u_{1\theta} = u_{1z} = p_1 = 0$ on the axis. To avoid singularity on the axis, the equations are multiplied by r^2 before taking the variational form. For the computation of the base flow, the finite elements formulation employs the higher-order Lagrange P3 and P2 elements for velocity and pressure, respectively. For the linear stability analysis, instead, P2 and P1 elements are used.

3. The symmetry-breaking bifurcation

3.1. Base flow

The axisymmetric low-Re base flow for the four considered geometries is shown in figures 3 and 4 at $Re = Re_c$, corresponding to the first onset of the symmetry-breaking instability, for $\mathcal{R} = 1$ and 4. Only a brief characterisation is provided here, as the effect of the different placement of the corners resembles what was found by Chiarini *et al.* (2022) for 2-D symmetric bodies.

A shear layer with negative azimuthal vorticity $\omega_{0\theta}$ separates from the rear part of the body and delimits the axisymmetric wake recirculation region. The vorticity is maximum in the vicinity of the body surface: for cones and bicones, $\omega_{0\theta}$ is maximum close to the

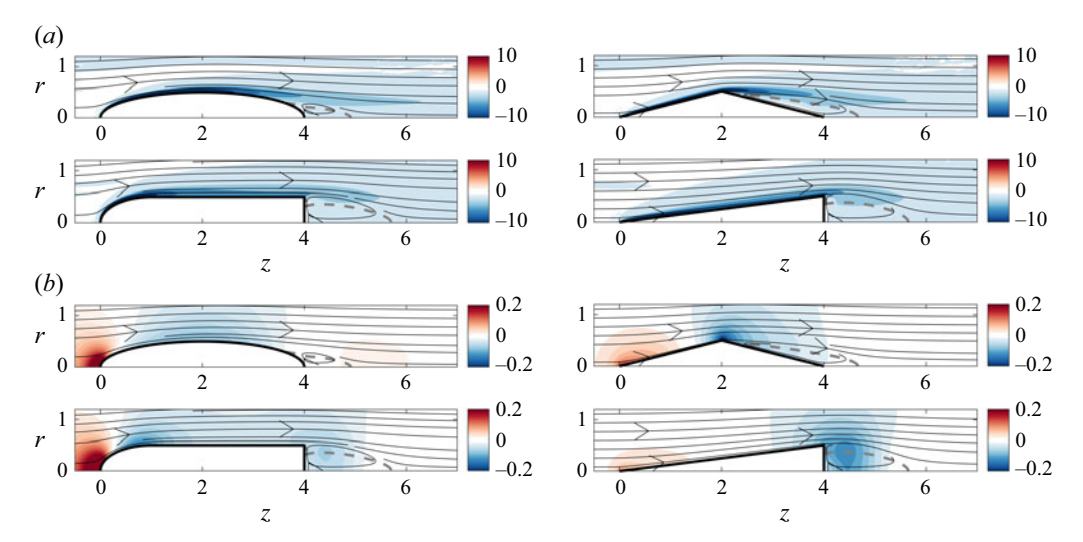


Figure 4. Same as figure 3 for $\mathcal{R}=4$. Ellipsoid, Re=1000; bicone, Re=775; bullet, Re=390; cone, Re=260.

corners, while for ellipsoids and bullets, the region with intense vorticity is more spread. The pressure distribution changes accordingly (see the bottom right panels in figures 3 and 4). For bodies with a blunt TE (cones and bullets), the minimum of the pressure is placed at the TE corners, and the flow streamlines along the lateral side of the body face a favourable pressure gradient. For bodies with zero-thickness TE (ellipsoids and bicones), instead, the pressure is minimum where the cross-stream size of the body is maximum. In this case, the flow streamlines along the lateral side of the body face first a favourable pressure gradient and then an adverse one that promotes the flow separation. Notably, the adverse pressure gradient becomes milder as \mathcal{R} increases. For cones and bullets, the flow separation point is set by the geometry at the TE corner. The cross-stream dimension of the wake recirculation region is thus determined by the body width, and its extent only slightly decreases with \mathcal{R} . On the contrary, for ellipsoids and bicones, the flow separation is driven by the pressure distribution (see figures 3 and 4). In agreement with the milder pressure gradient, the separation point moves downstream for larger \mathcal{R} , yielding a thinner and shorter wake recirculation region (see also figure 19 in Appendix A).

3.2. Neutral curves

We now move to the results of the linear stability analysis. Figure 5 shows the neutral curves for the primary instability that, for all cases, consists in the regular ($\lambda_i = 0$) symmetry-breaking bifurcation of an eigenmode of azimuthal wavenumber m = 1. Table 1 compares the results of our computations with those of Meliga *et al.* (2009*b*) and Bohorquez *et al.* (2011) for validation purposes. We find very good agreement with the results of Meliga *et al.* (2009*b*), while some discrepancies are observed when comparing with Bohorquez *et al.* (2011) (we measure a relative difference in the value of Re_c of approximately 4% for R = 6). We conjecture that this discrepancy is due to the different numerical method and to the different size of the computational domain.

Looking at figure 5, a first observation is that although the primary bifurcation is the same for the different bodies, the value of Re_c shows large variability, with $Re_c \approx 150$ for the $\mathcal{R}=1$ bicone, and $Re_c \approx 1400$ for the $\mathcal{R}=5$ ellipsoid. This highlights that U_{∞} and H are not the appropriate velocity and length scales for the characterisation and prediction of

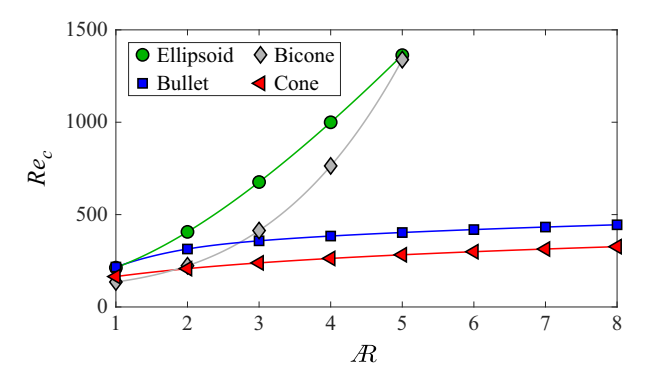


Figure 5. Critical Reynolds number as a function of the aspect ratio.

Body	Ellipsoid		Bullet				
\mathcal{R}	1	1	2	3	4	5	6
Meliga <i>et al.</i> (2009b)	213	_	_	_	_	_	_
Bohorquez et al. (2011)	_	216	327	372	399	420	435
Present study	213	216	314	358	384	403	419

Table 1. Comparison of the critical Reynolds number Re_c with results from the literature, for some geometries.

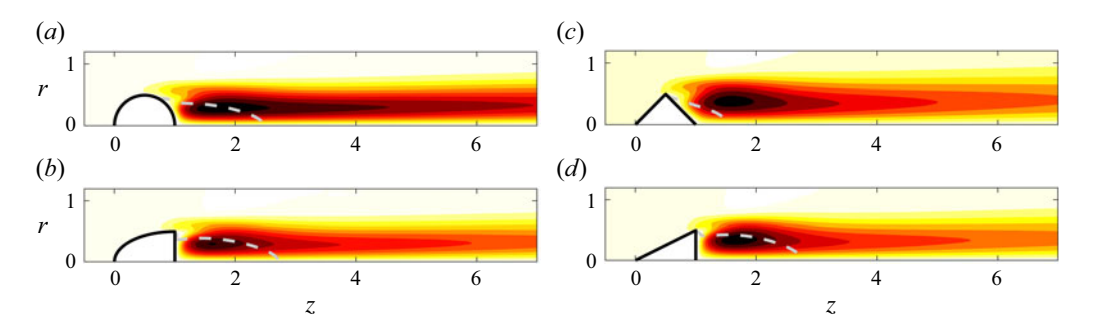


Figure 6. Eigenmode for $\mathcal{R}=1$ at $Re\approx Re_c$: streamwise velocity. Ellipsoid, Re=210; bicone, Re=135; bullet, Re=220; cone, Re=160. Dashed line: $u_{0z}=0$.

this bifurcation. Similarly to the flow past 2-D symmetric cylinders (Chiarini *et al.* 2022), an increase in the aspect ratio leads to a stabilisation of the base flow regardless of the body geometry; see in figure 5 that Re_c increases monotonically with \mathcal{R} . This effect holds also for non-axisymmetric bodies, as shown e.g. by Zampogna & Boujo (2023) and Chiarini & Boujo (2025) in the context of 3-D rectangular prisms. Notably, the way Re_c varies with \mathcal{R} depends on the shape of the TE of the body. For bodies with a blunt TE (cones and bullets), the critical Reynolds number almost flattens as \mathcal{R} increases. For bodies with zero-thickness TE (ellipsoids and bicones), instead, the critical Reynolds number increases faster than linearly, and very large values of Re_c are observed already at intermediate \mathcal{R} . An explanation for the steep increase of Re_c with \mathcal{R} for bodies with zero-thickness TE is provided in § 4.

For completeness, we show in figures 6 and 7 the axial velocity of the unstable mode for different geometries. Qualitatively, the structure of the mode does not change among the considered geometries, and agrees with the results of other authors; see e.g. figure 8 of

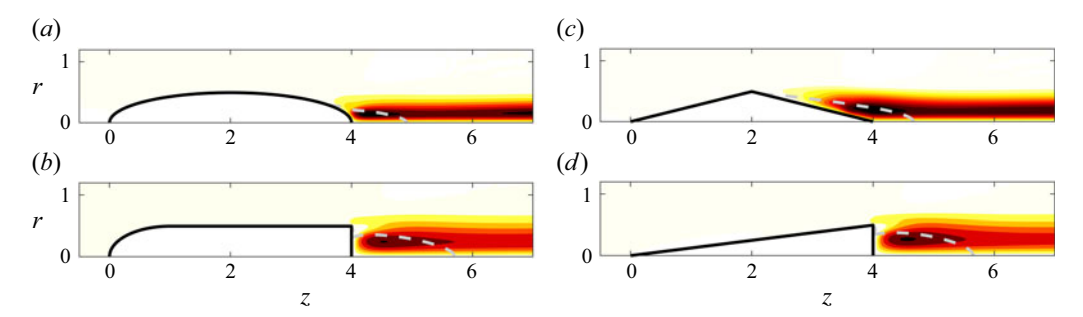


Figure 7. Same as figure 6 for $\mathcal{R}=4$. Ellipsoid, Re=1000; bicone, Re=775; bullet, Re=390; cone, Re=260.

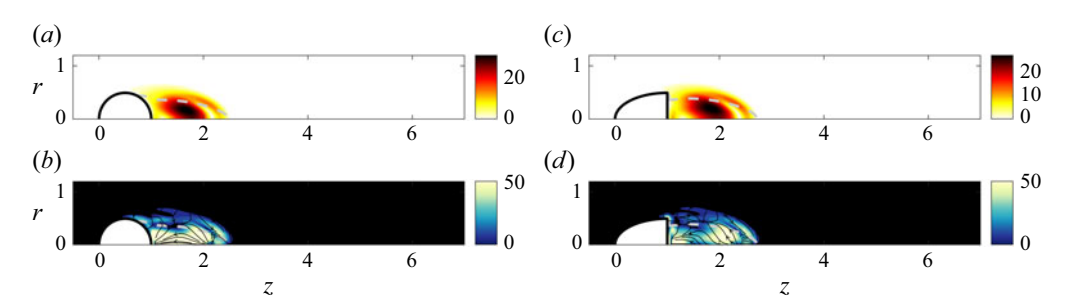


Figure 8. Spatial distribution of the (a,c) structural sensitivity S and (b,d) sensitivity of the growth rate to base-flow modification $\nabla_{u_0} \lambda_r$ for $\mathcal{R} = 1$ at $Re \approx Re_c$. Panels (a,b) are for the ellipsoid at Re = 210. Panels (c,d) are for the bullet at Re = 220. Dashed line: $u_{0z} = 0$.

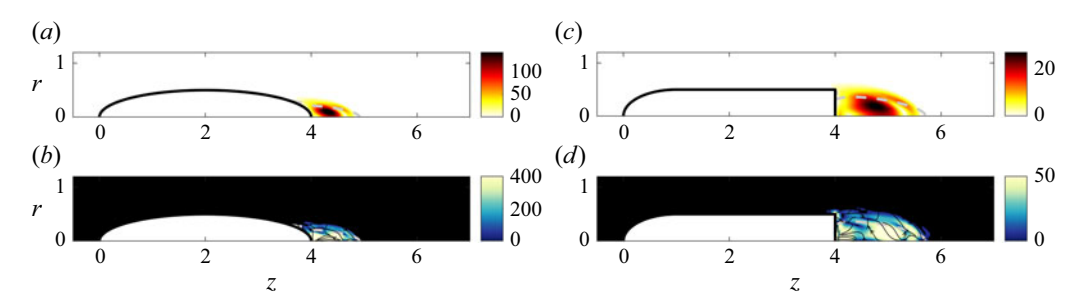


Figure 9. Same as figure 8 for $\mathcal{R} = 4$. Ellipsoid, Re = 1000; bullet, Re = 390.

Natarajan & Acrivos (1993) and figure 4 of Meliga *et al.* (2009*a*). The perturbation field is confined in the wake, with the largest value found close to the TE of the body within the wake recirculation region. This is consistent with the appearance of a pair of streamwise counter-rotating vortices in the wake (see the discussion in § 1), and with the instability mechanism discussed in § 4. For bodies with zero-thickness TE, the region where the mode is intense extends farther downstream.

3.3. Sensitivities

To further characterise the instability, we consider in figures 8 and 9 the structural sensitivity (Giannetti & Luchini 2007) and the sensitivity to base-flow modifications (Marquet, Sipp & Jacquin 2008; Meliga, Sipp & Chomaz 2010). For brevity, here we show only ellipsoids and bullets, being representative of bodies with zero-thickness TE and with a blunt base.

The structural sensitivity S(x) is based on the interplay between the direct and adjoint modes, and identifies the region where a generic structural modification of the stability problem provides the largest drift of the leading eigenvalue. It is an upper bound for the eigenvalue variation $|\delta\lambda|$ induced by a local body force actuation proportional to the signal of a velocity sensor located at the exact same station. The region of the flow where S is large identifies the wavemaker (Monkewitz, Huerre & Chomaz 1993). For the primary instability, the structural sensitivity is defined as

$$S(\mathbf{x}) = \frac{\|\hat{\boldsymbol{u}}_{1}^{\dagger}\| \|\hat{\boldsymbol{u}}_{1}\|}{\langle \hat{\boldsymbol{u}}_{1}^{\dagger}, \hat{\boldsymbol{u}}_{1} \rangle}, \tag{3.1}$$

where $\|\cdot\|$ represents the R^2 Euclidean norm, $\hat{\boldsymbol{u}}_1^{\dagger}$ is the adjoint mode, and $\langle \boldsymbol{u}_A, \boldsymbol{u}_B \rangle = \int_D \boldsymbol{u}_A^* \cdot \boldsymbol{u}_B \, \mathrm{d}\Omega$ is the inner product of $L^2(D)$, with the superscript * denoting the complex conjugate. For all cases, $S(\boldsymbol{x})$ is substantially close to zero everywhere except close to the body where the product of the direct and adjoint modes is large. Large values are observed along the separation line $u_{0z} = 0$ and within the recirculating region, where the maximum is observed (Meliga *et al.* 2009b). The similar distribution of $S(\boldsymbol{x})$ suggests that the different geometries and \mathcal{R} values considered share the same wavemaker and the same instability mechanism, which are spatially located within the recirculating region. Note that for bodies with zero-thickness TE, the spatial extent of the wavemaker decreases as \mathcal{R} increases, in agreement with the smaller recirculating region and with the base-flow stabilisation.

Next, the sensitivity to base-flow modifications quantifies the variation of the complex eigenpair $(\lambda, \hat{u}_1, \hat{p}_1)$ induced by a small variation of the base flow δu_0 . Specifically, the variation of the eigenvalue $\delta \lambda$ is linked with δu_0 by the inner product $\delta \lambda = \langle \nabla_{u_0} \lambda, \delta u_0 \rangle$, where

$$\nabla_{\mathbf{u}_0} \lambda = \frac{-(\nabla \hat{\mathbf{u}}_1)^H \cdot \hat{\mathbf{u}}_1^{\dagger} + \nabla \hat{\mathbf{u}}_1^{\dagger} \cdot \hat{\mathbf{u}}^*}{\langle \hat{\mathbf{u}}_1^{\dagger}, \hat{\mathbf{u}}_1 \rangle}$$
(3.2)

is indeed the sensitivity of λ to base-flow modifications; here, the superscript H indicates the trans-conjugate. The variation of the growth rate induced by δu_0 is thus expressed as $\delta \lambda_r = (\nabla_{u_0} \lambda_r, \delta u_0)$, where the corresponding sensitivity is $\nabla_{u_0} \lambda_r = \text{Re}(\nabla_{u_0} \lambda)$. Unlike the structural sensitivity S, which is a scalar field, the sensitivity $\nabla_{u_0} \lambda_r$ to base-flow modification is a vector field: the field lines provide the local orientation of the sensitivity field, while the magnitude provides the intensity. As expected, far from the bodies, $\nabla_{u_0} \lambda_r$ decays to zero due to the spatial separation of the direct and adjoint modes. Large values are instead observed close to the $u_{0z} = 0$ line and within the recirculating region. For bodies with zero-thickness TE, $\nabla_{u_0} \lambda_r$ is large within the entire recirculating region, while for bodies with a blunt base, the sensitivity is maximum at the downstream end of the recirculating region, close to the base and in correspondence with the corners (this resembles what is observed for 2-D rectangular cylinders; see Chiarini, Quadrio & Auteri 2021). For all cases, an increase of the backflow within the recirculating region ($\delta u_{0z} < 0$) largely destabilises the flow. Again, for bodies with zero-thickness TE, the spatial extent where the sensitivity is large decreases with R.

3.4. Effect of the Reynolds number

We now investigate the effect of a small variation of Re on the growth rate λ_r . We start by looking for an expression for $\partial \lambda_r / \partial Re$. We consider a small departure from criticality

such that

$$\frac{1}{Re_c} - \frac{1}{Re} = \varepsilon,\tag{3.3}$$

where $|\varepsilon| \ll 1$ ($\varepsilon < 0$ for $Re < Re_c$, and $\varepsilon > 0$ for $Re > Re_c$). A small-amplitude change in Re induces small changes in the base flow, in the eigenmode and in the eigenvalues, i.e.

$$\{u_0, p_0\} \rightarrow \{u_0, p_0\} + \{\delta u_0, \delta p_0\}, \quad \{\hat{u}_1, \hat{p}_1\} \rightarrow \{\hat{u}_1, \hat{p}_1\} + \{\delta \hat{u}_1, \delta \hat{p}_1\}, \quad \lambda \rightarrow \lambda + \delta \lambda.$$
(3.4)

We now set $Re = Re_c$ as reference, and inject these changes into the steady nonlinear NS equations and into the linearised NS equations. By keeping the first-order terms only, we then obtain the equations for the base-flow modification $\{\delta \boldsymbol{u}_0, \delta p_0\}$ and for the eigenmode modification $\{\delta \hat{\boldsymbol{u}}_1, \delta \hat{p}_1\}$, i.e.

$$\begin{pmatrix} \mathcal{L}_0\{\boldsymbol{u}_0, Re_c\}(\boldsymbol{\cdot}) & \nabla_0(\boldsymbol{\cdot}) \\ \nabla_0 \boldsymbol{\cdot} (\boldsymbol{\cdot}) & 0 \end{pmatrix} \begin{pmatrix} \delta \boldsymbol{u}_0 \\ \delta p_0 \end{pmatrix} = \begin{pmatrix} -\varepsilon \nabla_0^2 \boldsymbol{u}_0 \\ 0 \end{pmatrix}$$
(3.5)

and

$$\lambda \begin{pmatrix} \mathcal{I} & \mathbf{0} \\ \mathbf{0}^{\mathsf{T}} & 0 \end{pmatrix} \begin{pmatrix} \delta \hat{\boldsymbol{u}}_1 \\ \delta \hat{p}_1 \end{pmatrix} + \begin{pmatrix} \mathcal{L}_m \{\boldsymbol{u}_0, Re_c\}(\boldsymbol{\cdot}) & \nabla_m(\boldsymbol{\cdot}) \\ \nabla_m \boldsymbol{\cdot} (\boldsymbol{\cdot}) & 0 \end{pmatrix} \begin{pmatrix} \delta \hat{\boldsymbol{u}}_1 \\ \delta \hat{p}_1 \end{pmatrix} = \begin{pmatrix} \mathcal{F}_m (\delta \boldsymbol{u}_0, \hat{\boldsymbol{u}}_1) \\ 0 \end{pmatrix}, \quad (3.6)$$

accompanied by homogeneous Dirichlet boundary conditions at the inlet and at the surface of the body, and stress-free conditions at the outlet and at the far field; here,

$$\mathcal{F}_m(\delta \mathbf{u}_0, \hat{\mathbf{u}}_1) = -\mathcal{C}_m(\hat{\mathbf{u}}_1, \delta \mathbf{u}_0) - \varepsilon \nabla_m^2 \hat{\mathbf{u}}_1 - \delta \lambda \hat{\mathbf{u}}_1. \tag{3.7}$$

Equation (3.5) is divided by ε and solved for $\boldsymbol{u}_0^{\varepsilon} = \delta \boldsymbol{u}_0/\varepsilon$. Equation (3.6) is projected on the adjoint mode $\{\hat{\boldsymbol{u}}_1^{\dagger}, \hat{p}_1^{\dagger}\}$ to eliminate $\{\delta \hat{\boldsymbol{u}}_1, \delta \hat{p}_1\}$ and obtain an expression for $\delta \lambda$, i.e.

$$\delta \lambda = -\varepsilon \frac{\langle \hat{\boldsymbol{u}}_{1}^{\dagger}, C_{m}(\hat{\boldsymbol{u}}_{1}, \boldsymbol{u}_{0}^{\varepsilon}) + \nabla_{m}^{2} \hat{\boldsymbol{u}}_{1} \rangle}{\langle \hat{\boldsymbol{u}}_{1}^{\dagger}, \hat{\boldsymbol{u}}_{1} \rangle}.$$
(3.8)

Interestingly, this expression matches exactly the one for the linear coefficient of the amplitude equation obtained with a standard weakly nonlinear stability analysis (Sipp & Lebedev 2007; Zampogna & Boujo 2023). At this point, we can write the $\partial \lambda_r / \partial Re$ derivative as

$$\frac{\partial \lambda_r}{\partial Re} = \frac{\partial \lambda_r}{\partial \varepsilon} \frac{\partial \varepsilon}{\partial Re} = \frac{1}{Re^2} \frac{\partial \lambda_r}{\partial \varepsilon} = -\frac{1}{Re^2} \operatorname{Re} \left(\frac{\langle \hat{\boldsymbol{u}}_1^{\dagger}, \mathcal{C}_m(\hat{\boldsymbol{u}}_1, \boldsymbol{u}_0^{\varepsilon}) + \nabla_m^2 \hat{\boldsymbol{u}}_1 \rangle}{\langle \hat{\boldsymbol{u}}_1^{\dagger}, \hat{\boldsymbol{u}}_1 \rangle} \right). \tag{3.9}$$

A small change in the Reynolds number thus leads to a modification of the growth rate that depends on the effect of the base-flow modification on the eigenmode, i.e. $\langle \hat{\pmb{u}}_1^{\dagger}, \mathcal{C}_m(\hat{\pmb{u}}_1, \pmb{u}_0^{\varepsilon}) \rangle$, and on the direct effect of Re on the viscous term of the eigenmode, i.e. $\langle \hat{\pmb{u}}_1^{\dagger}, \nabla_m^2 \hat{\pmb{u}}_1 \rangle$. The spatial distribution of the integrand in the inner product of (3.9) provides information regarding the region that contributes most to the increase of the growth rate when Re increases (recall that we set $Re = Re_c$ as reference such that here $\partial \lambda_r / \partial Re > 0$).

Figure 10 shows the results for the ellipsoid and the bullet with $\mathcal{R}=1$. Figures 10(a,c) show the modification of the base-flow azimuthal vorticity $\omega_{0\theta}^{\varepsilon}$ (to be compared with figure 3). For all considered geometries, the ε Reynolds increase leads to a more negative vorticity in the layer along the separating streamline, and to a more positive vorticity in the base region and in a tiny elongated region along the $u_{0z}=0$ line. Interestingly, the latter region closely matches the region where $\partial \omega_{0\theta}/\partial r$ first changes sign (see the

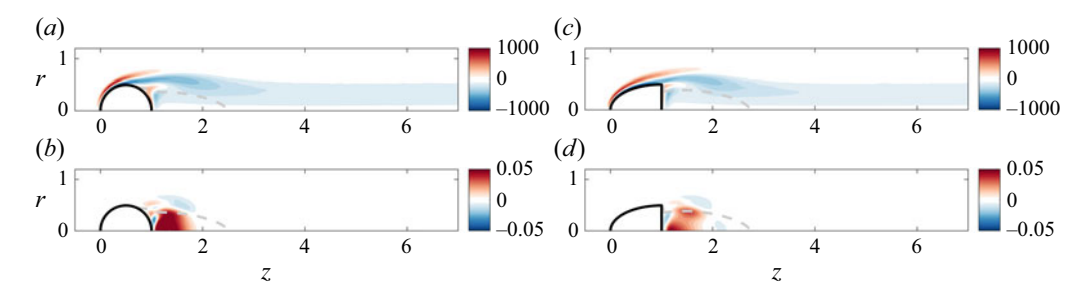


Figure 10. Effect of a small increase in Re on the base flow and on the growth rate for $\mathcal{R}=1$ at $Re \approx Re_c$. Panels (a,c) show the spatial distribution of $\omega_{\theta,0}^e$. Panels (b,d) show the spatial distribution of the integrand of $\delta \lambda_r$ (see text and (3.9)). Panels (a,b): ellipsoid, Re=210. Panels (c,d): bullet, Re=220. Dashed line: $u_{0z}=0$.

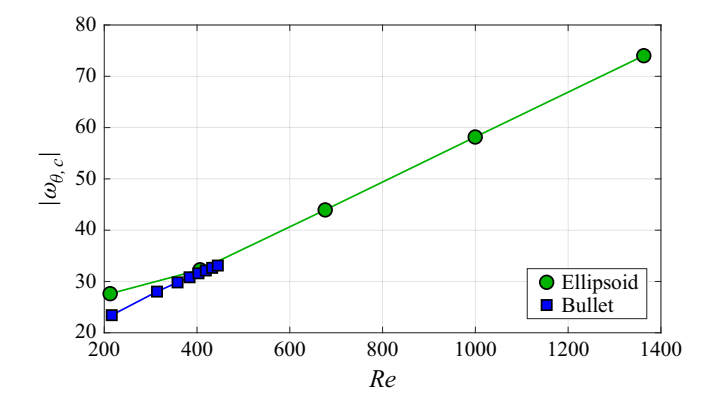


Figure 11. Maximum surface azimuthal vorticity at $Re = Re_c$.

discussion in § 4). Figures 10(b,d) show the integrand of the inner product in (3.9), and reveal that the destabilisation due to the increase of Re mostly comes from the upstream region of the recirculating region, which closely matches the wavemaker identified by the structural sensitivity. Moreover, a close inspection of the terms in (3.9) shows that almost the complete destabilisation is due to the convective-like term resulting from the base-flow modification rather than due to the direct effect of Re on the eigenmode, as $|\hat{u}_1^{\dagger*} \cdot \mathcal{C}_m(\hat{u}_1, u_0^{\epsilon})| \gg |\hat{u}_1^{\dagger*} \cdot \nabla_m^2 \hat{u}_1|$ at all positions (not shown).

4. Azimuthal vorticity and mechanism of the primary bifurcation

In this section, we show that the instability mechanism proposed by MM for oblate spheroidal objects with a free-slip surface extends to axisymmetric bodies with a no-slip surface.

4.1. Maximum surface vorticity

As discussed in § 1, the MM arguments are based on the idea that the bifurcation is driven by the vorticity generated at the body surface and transported into the wake. Therefore, we start by assessing the relation between the base-flow surface vorticity and the onset of the bifurcation. To simplify the notation, in this and in the following subsection (§ 4.2), we drop the 0 subscript. Introducing $\omega_{\theta,max}(Re)$ as the maximum vorticity measured on the surface of a body of given geometry and aspect ratio, figure 11 shows $\omega_{\theta,c}(Re)$, i.e. the maximum surface vorticity $\omega_{\theta,max}$ at the critical Reynolds number $Re = Re_c$. We report values for the ellipsoids and bullets, which have a smooth geometry. For cones

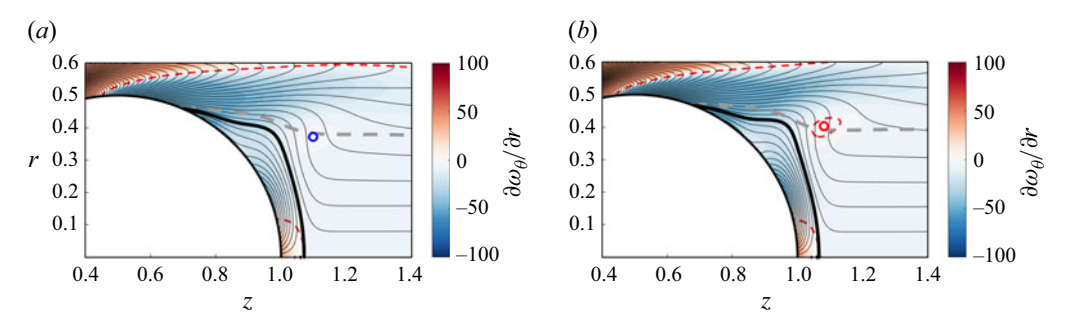


Figure 12. Near-wake distribution of the azimuthal vorticity around an ellipsoid with no-slip surface and $\mathcal{R}=1$, for (a) $Re=250<\widetilde{Re}$, (b) $Re=290>\widetilde{Re}$, where \widetilde{Re} is the Reynolds number corresponding to the first appearance of a region with $\partial\omega_{\theta}/\partial r \geqslant 0$ with $\omega_{\theta}<0$. Thin black lines are isocontours of the azimuthal vorticity ω_{θ} . The thick black line delimits the 'boundary layer' where $\omega_{\theta}>0$. Coloured contours show $\partial\omega_{\theta}/\partial r$. The grey dashed line shows $u_z=0$, and the red dashed line shows $\partial\omega_{\theta}/\partial r=0$. Blue/red circles indicate the negative/positive maxima of $\partial\omega_{\theta}/\partial r$ in the near-wake region.

and bicones, we note that the maximum surface vorticity diverges at the sharp edges, which leads to $\omega_{\theta,max}$ growing unboundedly when refining the numerical mesh, while the critical Reynolds number is well converged. It is therefore unlikely that a simple relationship between $\omega_{\theta,max}$ and Re_c holds for bodies with a sharp geometry. See Appendix C for more details.

Similarly to what was observed by MM for free-slip surfaces, figure 11 shows that $\omega_{\theta,c}$ has a linear dependence on Re, and that the results for the two considered geometries collapse rather well onto the same curve:

$$\omega_{\theta,c}(Re) \approx a + bRe,$$
 (4.1)

where a and b are two constants. The amount of vorticity that has to be produced at the body surface to promote the flow instability increases linearly with the Reynolds number, in a way that does not depend on the geometry of the body. This provides a simple criterion for predicting the onset of the instability, which requires only the knowledge of the maximum azimuthal vorticity at the surface (which is, however, not always easily available, as discussed later, in § 5): at a given Reynolds number, the flow is stable when $\omega_{\theta,max}(Re) < \omega_{\theta,c}(Re)$, and unstable when $\omega_{\theta,max}(Re) > \omega_{\theta,c}(Re)$. The linear fit of our data with (4.1) gives a = 14 and $b = 4.4 \times 10^{-2}$. These values differ from the constants a = 12.5 and $b = 4.3 \times 10^{-3}$ found by MM for ellipsoids with free-slip surface. This is expected, as the maximum surface vorticity at criticality depends on the slip at the body surface; see e.g. figure 4 of Legendre, Lauga & Magnaudet (2009) for the flow past a circular cylinder at different Knudsen numbers. Notably, the different values of b show that the critical vorticity at the body surface exhibits a faster variation with Re for axisymmetric bodies with a no-slip surface than for those with a free-slip surface.

4.2. Vorticity gradient

We now focus on the near-wake region, and investigate the correlation between the flow bifurcation and the appearance of points where $\partial \omega_{\theta}/\partial r=0$. Figure 12 shows the vorticity distribution in the near wake for the $\mathcal{R}=1$ ellipsoid (with the same representation as in figure 1). Due to the no-slip boundary condition, a thin boundary layer arises on the rear side of the body, where the azimuthal vorticity is positive, $\omega_{\theta}>0$, i.e. has the opposite sign as in the rest of the flow (the black thick line in figure 12 denotes $\omega_{\theta}=0$). Outside this boundary layer, the vorticity distribution closely resembles that of free-slip bodies: isocontours of ω_{θ} are essentially parallel to the solid surface in the vicinity of the body,

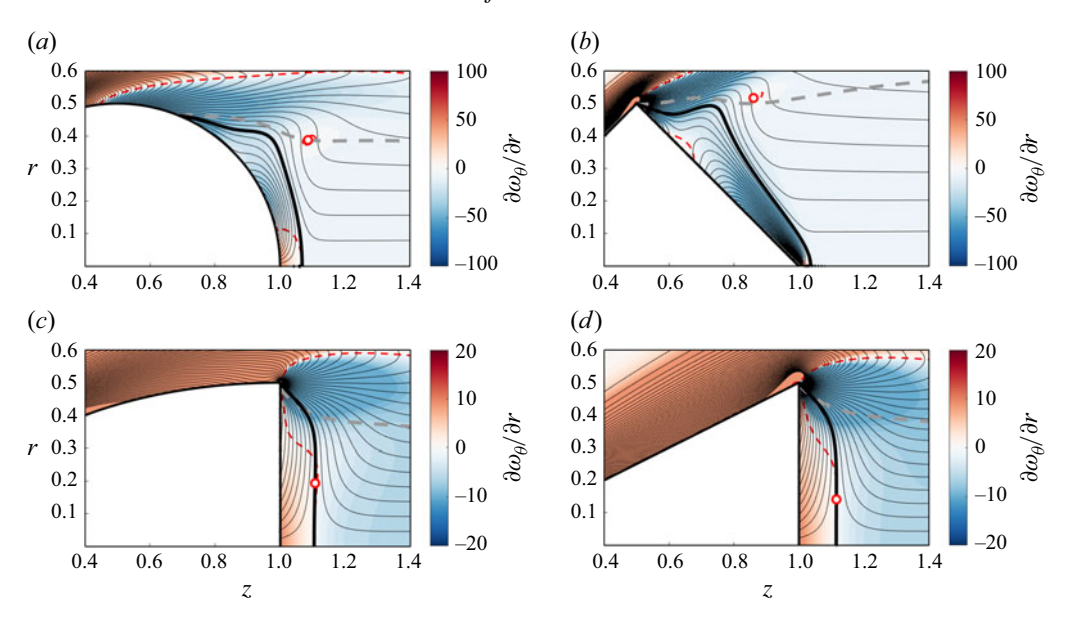


Figure 13. As figure 12 for the four considered geometries with $\mathcal{R}=1$. The Reynolds number is slightly above \widetilde{Re} , i.e. after the first appearance of a region with $\partial \omega_{\theta}/\partial r \geqslant 0$ where $\omega_{\theta} < 0$. Here, (a) ellipsoid at Re = 270, (b) bicone at Re = 295, (c) bullet at Re = 120, (d) cone at Re = 80.

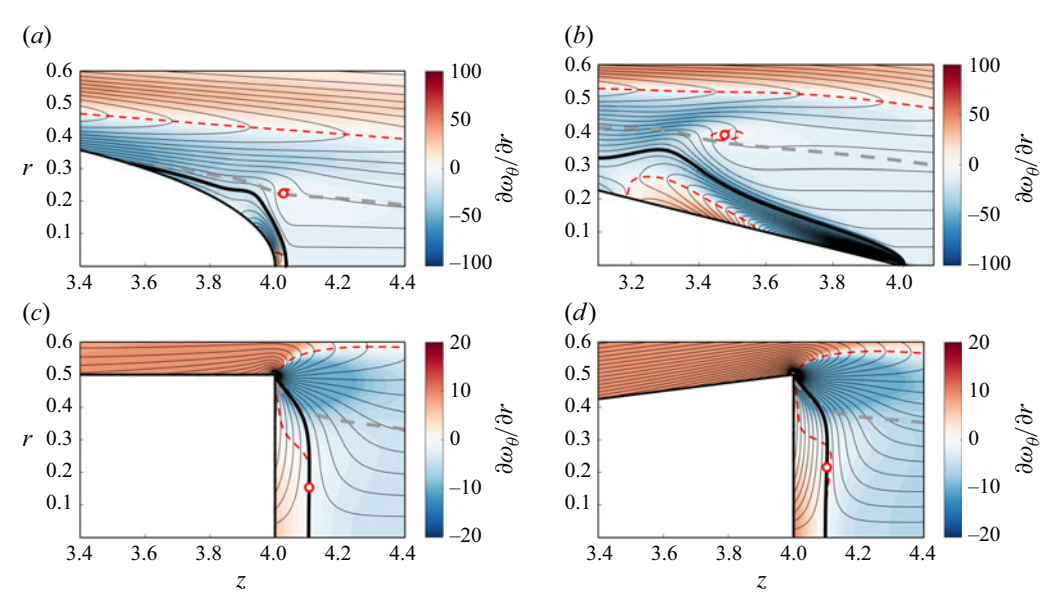


Figure 14. As figure 13 for R = 4, for (a) ellipsoid at Re = 1250, (b) bicone at Re = 950, (c) bullet at Re = 175, (d) cone at Re = 150.

and farther downstream, they align with the symmetry axis. In the transition region in between, the turning of the ω_{θ} isocontours becomes sharper and sharper as Re gets larger. Two values of the Reynolds number are considered in figure 12, one below (figure 12a) and one above (figure 12b) the critical Reynolds number Re_c . One can immediately notice that $\partial \omega_{\theta}/\partial r < 0$ (blue) everywhere in the transition region when $Re < Re_c$, while a region where $\partial \omega_{\theta}/\partial r \ge 0$ (red) appears when $Re > Re_c$, in agreement with the MM arguments. Figures 13 and 14 are as figure 12(b), for different geometries and aspect ratios. Notably,

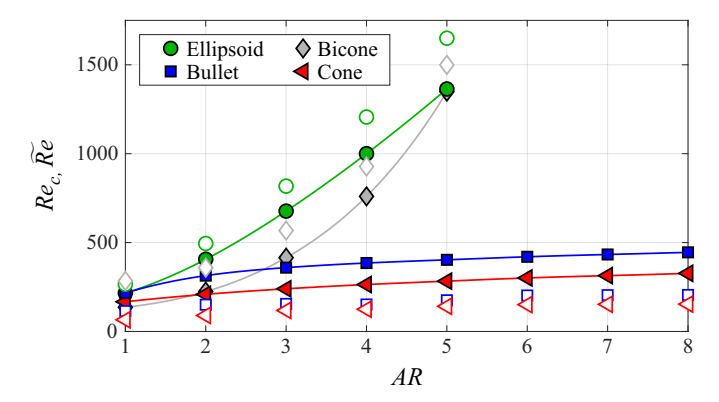


Figure 15. Critical Reynolds number Re_c (lines) and lowest Reynolds number \widetilde{Re} (open symbols) such that $\partial \omega_{\theta}/\partial r \geqslant 0$ with $\omega_{\theta} < 0$ in the near wake.

the location where the $\partial \omega_{\theta}/\partial r \geqslant 0$ region appears depends on the shape of the TE. For a blunt TE, it is placed along the $\omega_{\theta}=0$ isocontour delimiting the base boundary layer due to the no-slip boundary condition. For bodies with zero-thickness TE, instead, it is located farther downstream within the wake recirculation region, and close to the contour of zero streamwise velocity $u_z=0$.

It is worth noting that the vorticity distribution for bodies with zero-thickness TE explains the steep increase of Re_c with \mathcal{R} observed in figure 5. Due to the specific shapes of these bodies, the ω_{θ} isocontours close to the body surface become more aligned with the symmetry axis r=0 as \mathcal{R} increases. For these bodies, therefore, the condition $\partial \omega_{\theta}/\partial r=0$ (ω_{θ} isocontours being locally perpendicular to the symmetry axis) for the instability to occur requires more vorticity to be produced at the body surface, i.e. a larger Reynolds number.

Figure 15 quantifies the correlation between the onset of the instability and the first appearance of points where $\partial \omega_{\theta}/\partial r = 0$. We compare the critical Reynolds number Re_c obtained from our stability analysis with the Reynolds number Re_c corresponding to the first appearance of a point where $\partial \omega_{\theta}/\partial r = 0$ in the near wake (we consider only the near wake outside the boundary layer that develops along the TE). Although the collapse with Re_c is not perfect, Re_c captures the trend of the critical Reynolds number rather nicely for all the considered geometries, increasing sharply with Re_c for bodies with a zero-thickness TE, and much more slowly for bodies with a blunt TE.

To summarise, our results show that the instability mechanism proposed by MM in the context of ellipsoids with free-slip surfaces also extends to no-slip surfaces, and describes fairly well the primary symmetry-breaking bifurcation of the flow past axisymmetric bodies with different geometries and aspect ratios. This clearly hints to the fact that the vorticity generated at the body surface is at the root of the instability mechanism, while the way it is produced, i.e. the nature of the surface, does not play a major role.

4.3. Free-slip versus no-slip

It is worth spending few words on the fact that, as shown in the previous subsections, axisymmetric wakes past free-slip and no-slip bodies share the same instability mechanism. It is well known that the mechanism of vorticity generation on a surface changes with the boundary condition; see e.g. Truesdell (1954), Lighthill (1963), Morton (1984), Leal (1989), Wu & Wu (1993), Wu (1995), Lundgren & Koumoutsakos (1999), Brøns *et al.* (2014) and Terrington *et al.* (2020). This is clear when looking at the 'boundary vorticity flux' (normal diffusion flux of vorticity) at the surface, $\sigma = \nu n \cdot \nabla \omega$, which is a

measure of the vorticity creation at the wall. For stationary rigid walls, it reads (see Wu & Wu 1993)

$$\sigma = \underbrace{n \times \left(\frac{\nabla p}{\rho}\right)}_{\sigma_n} \underbrace{-(n \times \nabla) \cdot (\tau n)}_{\sigma_{\tau}}, \tag{4.2}$$

where $\tau = \nu \omega \times n$ is the tangential shear stress. Here, σ depends on the non-uniform distribution of the normal (σ_p) and shear (σ_τ) stresses. In the limit case of a 2-D flow $u(x, y) = (u_x, u_y, 0)$ near a stationary, no-slip flat wall of normal $n = e_y$, the boundary vorticity flux reduces to $\sigma = \sigma_p = -(1/\rho)(\partial p/\partial x)e_z$, while $\sigma_\tau = 0$ (Lighthill 1963). By contrast, on a free-slip surface, the vorticity appears as a consequence of the continuity of the tangent stresses and is non-null only in the case of curved surfaces; in the limit case of a 2-D stationary surface, $\omega = 2U\kappa$, where U is the tangential velocity and κ is the local curvature; accordingly, the boundary vorticity flux is non-null only for curved surfaces (see Wu 1995).

The fact that axisymmetric bodies with no-slip and free-slip surfaces exhibit the same instability mechanism means that although the vorticity is at the root of the instability, the way it is produced at the wall does not play a dominant role in the overall triggering mechanism (see also the discussion in MM). In other words, the flow becomes unstable once the amount of vorticity brought into the near wake is large enough, irrespective of the production mechanism. Clearly, the different vorticity creation mechanism has an impact on the critical Reynolds number and on the actual onset of the instability, as it influences the size of the wake recirculation region and the amount of vorticity brought into the wake. The different vorticity creation mechanism, indeed, leads to some substantial differences between no-slip and free-slip surfaces in terms of boundary vorticity dynamics (Moore 1963; Wu 1995). For large Reynolds numbers, dimensional analysis shows that: (i) in the no-slip case, a boundary vorticity flux $\sigma \sim O(1)$ is generated, which implies that the surface vorticity increases as $\omega \sim Re^{1/2}$; (ii) in the free-slip case, the boundary vorticity flux decreases as $\sigma \sim Re^{-1/2}$, and the amount of surface vorticity is independent of the Reynolds number, $\omega \sim O(1)$.

4.4. On the amplification mechanism

We now investigate the contribution of various physical mechanisms to the exponential growth of the mode in the linear regime ($Re \approx Re_c$). We start by looking at the energy equation for the perturbation u_1 (see Lanzerstorfer & Kuhlmann 2012). We sum (2.4) multiplied by \hat{u}_1^* with the complex conjugate of the same equation multiplied by \hat{u}_1 , and after some manipulation and using the incompressibility constraint, we obtain the equation for $\hat{u}_1 \cdot \hat{u}_1^*$, i.e.

$$2\lambda_{r}\hat{\boldsymbol{u}}_{1} \cdot \hat{\boldsymbol{u}}_{1}^{*} = \underbrace{-\{(\hat{\boldsymbol{u}}_{1} \otimes \hat{\boldsymbol{u}}_{1}^{*} + \hat{\boldsymbol{u}}_{1}^{*} \otimes \hat{\boldsymbol{u}}_{1}) : \nabla_{0}\boldsymbol{u}_{0}\}}_{\mathcal{P}} \underbrace{-\frac{1}{Re}\nabla_{0}^{2}(\hat{\boldsymbol{u}}_{1} \cdot \hat{\boldsymbol{u}}_{1}^{*})}_{\mathcal{D}}$$

$$\underbrace{-\nabla_{0} \cdot (\hat{p}_{1}\hat{\boldsymbol{u}}_{1}^{*} + \hat{p}_{1}^{*}\hat{\boldsymbol{u}}_{1})}_{\mathcal{T}_{p}} \underbrace{-\nabla_{0} \cdot (\boldsymbol{u}_{0}\hat{\boldsymbol{u}}_{1} \cdot \hat{\boldsymbol{u}}_{1}^{*})}_{\mathcal{A}} - \underbrace{\frac{2}{Re}\left(\nabla_{m}\hat{\boldsymbol{u}}_{1} : \nabla_{m}^{*}\hat{\boldsymbol{u}}_{1}^{*}\right)}_{\mathcal{E}}. \quad (4.3)$$

On the right-hand side, in order, we find the production term \mathcal{P} that accounts for the exchange of energy between the base flow and the perturbation, the viscous diffusion term \mathcal{D} , the pressure transport term \mathcal{T}_p , the advection associated with the base flow \mathcal{A} ,

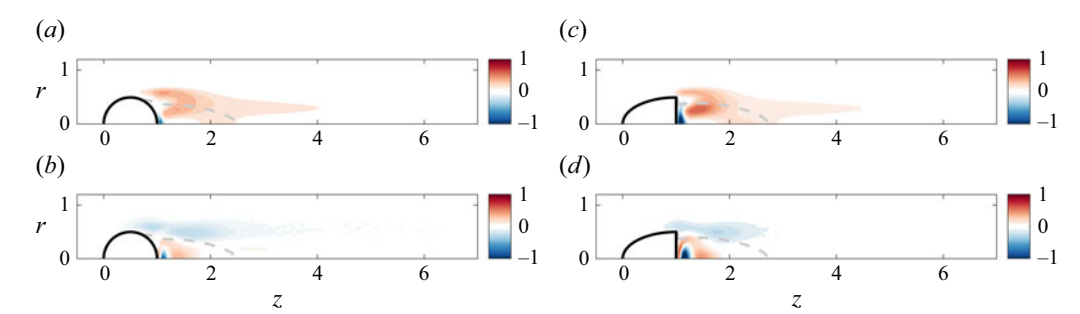


Figure 16. Energy budget for $\mathcal{R} = 1$ at $Re = Re_c$. Spatial distribution of the (a,c) production term \mathcal{P} and (b,d) advection term \mathcal{A} . Panels (a,b) are for the ellipsoid at Re = 210. Panels (c,d) are for the bullet at Re = 220. Dashed line: $u_{0r} = 0$.

and the viscous dissipation \mathcal{E} . All the terms contribute to the total budget, but differently depending on the flow region.

Figure 16 considers the energy equation for the ellipsoid and the bullet with $\mathcal{R}=1$ at $Re = Re_c$. In this case, $\lambda_r = 0$ and the Reynolds–Orr equation reduces to $\int_D \mathcal{P} d\Omega =$ $\int_D \epsilon d\Omega$, with $\int_D A + \mathcal{T}_p + \mathcal{D} = 0$. We focus on the spatial distribution of \mathcal{P} and \mathcal{A} to locate the flow regions where the mode amplification is driven by the production and/or the advection. We observe that $\mathcal{P} > 0$ downstream of the bodies, with the maximum placed along the separating streamline and within the recirculating region, where the base-flow velocity gradient is indeed maximum. At the base, the small $\mathcal{P} < 0$ region indicates that energy is moved from the perturbation to the base flow there. For bodies with a blunt base, we observe a more intense production activity, in agreement with the stronger base-flow velocity gradients. The advection term A, instead, behaves differently depending on the direction of u_0 . It is a sink (A < 0) and tends to stabilise the flow along the separating shear layer where $u_{0z} > 0$, while it is a source (A > 0) and tends to destabilise the flow within the recirculating region where $u_{0z} < 0$. In the recirculating region, the base flow transports the perturbations backwards in the near wake so that they can grow more compared to the situation where they are advected downstream. Note that this agrees with § 3.4, where the effect of a small increase in Re on λ_r is discussed (see in figure 10 the large positive $\partial \lambda_r / \partial Re > 0$ region in the core of the recirculating region).

Similar conclusions can be drawn by using the concept of endogeneity introduced by Marquet & Lesshafft (2015). The endogeneity E(x) characterises the contributions of localised flow regions to the global dynamics of the eigenmode, and allows us to separate the contributions from individual mechanisms such as production, base-flow advection, pressure forces and viscous diffusion. The endogeneity is defined as $E(x) = \hat{u}_1^{\dagger *} \cdot (-\mathcal{L}_m \hat{u}_1 - \nabla_m \hat{p}_1)$, and has the property that its integral equals the eigenvalue, i.e $\int_D E(x) d\Omega = \lambda$. We now replace the definition of \mathcal{L}_m in the above relation to obtain

$$E(\mathbf{x}) = -\hat{\mathbf{u}}_{1}^{\dagger *} \cdot ((\mathbf{u}_{0} \cdot \nabla_{m})\hat{\mathbf{u}}_{1}) - \hat{\mathbf{u}}_{1}^{\dagger *} \cdot ((\hat{\mathbf{u}}_{1} \cdot \nabla_{m})\mathbf{u}_{0}) - \hat{\mathbf{u}}_{1}^{\dagger *} \cdot \nabla \hat{p}_{1} + \frac{1}{Re} \, \hat{\mathbf{u}}_{1}^{\dagger *} \cdot \nabla_{m}^{2} \hat{\mathbf{u}}_{1}, \tag{4.4}$$

where, in order, the different terms account for the contribution of the base-flow advection, the production due to the base-flow velocity gradients, pressure forces and viscous diffusion. The real part of the endogeneity and of (4.4) isolates the contributions to the growth rate λ_r , while the imaginary part isolates the contributions to the eigenfrequency λ_i . Figure 17 shows the production and advection contribution to Re(E(x)) for the ellipsoid and the bullet with $\mathcal{R}=1$ at $Re=Re_c$. The endogeneity is concentrated close to the

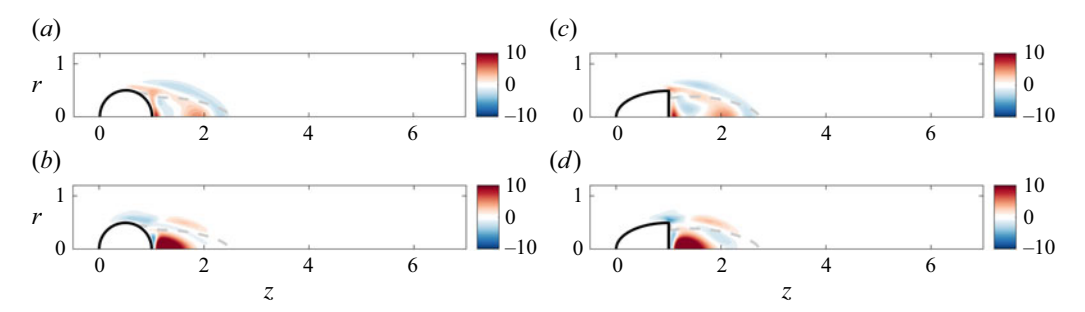


Figure 17. Spatial distribution of the (a,c) production and (b,d) advection contributions to the endogeneity for $\mathcal{R}=1$ and $Re \approx Re_c$. Panels (a,b) are for the ellipsoid at Re=210. Panels (c,d) are for the bullet at Re=220. Dashed line: $u_{0z}=0$.

body around the shear layers and within the recirculating region. The production has a stabilising/destabilising effect depending on the region, with the positive contribution to Re(E(x)) being maximum at the centre of the recirculating region. The advection, instead, has a strongly destabilising effect within the recirculating region where $u_{0z} < 0$, but a stabilising effect in the first portion of the shear layers separating from the bodies where $u_{0z} > 0$. This partially agrees with the energy budget analysis.

5. A new scaling

In the previous section, we have shown that the base-flow azimuthal vorticity drives the primary instability of the flow past 3-D axisymmetric bodies. We now use this information to define a new Reynolds number that is more suitable for predicting the onset of the instability than the standard Reynolds number based on U_{∞} and H. This is done in the same way as by Chiarini et al. (2022), who proposed a new scaling for the description of the primary instability of the flow past 2-D symmetric bluff bodies. They used a measure of the spatial extent of the separation bubble as a length scale, and the largest reverse flow speed within it as the velocity scale, and found that the ensuing Reynolds number evaluated at criticality only marginally changed with the geometry and aspect ratio of the body. This choice of scales was inspired by their link to the local amplification of the unstable wave packets and to the extension of the absolute instability region (Hammond & Redekopp 1997; Chomaz 2005). Here, we introduce a new scaling that can be used to estimate whether the low-Re steady flow past axisymmetric bodies is unstable, without the need for a computationally expensive stability analysis. This new scaling is based on the inspection of the base flow only (here we again drop the 0 subscript), and relies on quantities that are related to the physics of the problem and are easily accessible in both experiments and numerical simulations.

The onset of the primary symmetry-breaking bifurcation depends on the thickness of the transition region where the instability mechanism takes place (see § 4). A thinner transition region, indeed, means that the ω_{θ} isocontours exhibit sharper turnings, and points with $\partial \omega_{\theta}/\partial r = 0$ are more likely to arise. The thickness of this region depends on (i) the maximum vorticity $\omega_{\theta,max}$ generated at the body surface (see figure 11), and (ii) the radial extent of the wake recirculation region (see MM). Thus one may be tempted to use $\omega_{\theta,max}$ and a measure of r_0 to define a new Reynolds number. However, the measure of $\omega_{\theta,max}$ at the body surface is not always available. First, vorticity diverges at a geometric singularity such as a sharp leading edge, as observed for cones and bicones. Second, in experiments, the flow region close to the body surface is not easily

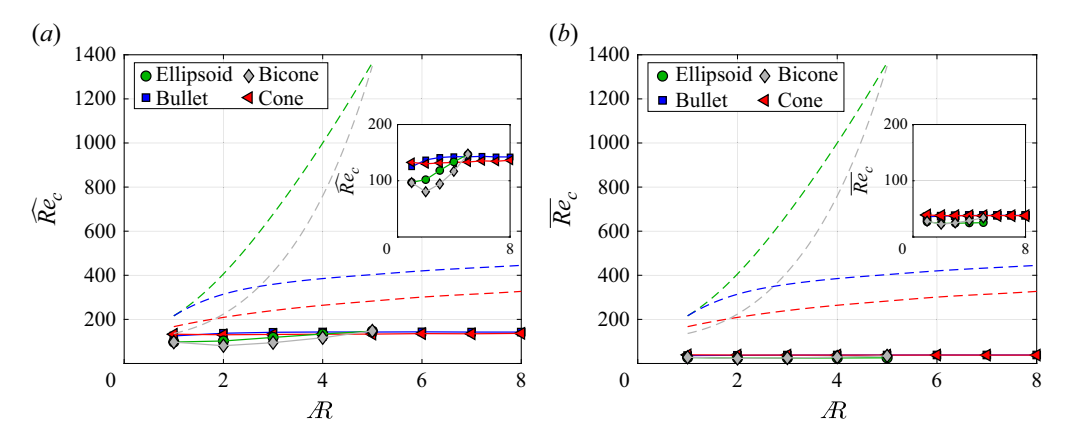


Figure 18. Critical Reynolds number Re_c (dashed lines) and newly defined Reynolds numbers (solid lines): (a) $\widehat{Re}_c = \widetilde{\omega}_\theta r_0^2 / \nu$, (b) $\overline{Re}_c = U_{rev} r_0 / \nu$.

accessible. A different estimation of the surface vorticity is thus needed. Here, we propose $\widetilde{\omega}_{\theta} = \max_r (\omega_{\theta}(r, z_{max}))$, where z_{max} is the streamwise location of maximum reverse flow U_{rev} within the wake recirculation region. We use $\widetilde{\omega}_{\theta}$ as a vorticity-related scale, and the radius of the $u_z = 0$ isocontour at the same z_{max} streamwise location as a measure of r_0 , and define the new Reynolds number as $\widehat{Re} = \widetilde{\omega}_{\theta} r_0^2 / \nu$. Figure 18(a) shows that at criticality, this new Reynolds number Re collapses approximately to the same value for all the considered bodies. The collapse is not perfect, yet the relative variation is one order of magnitude smaller than that observed with the standard Reynolds number based on U_{∞} and H. To be quantitative, we measure e.g. $Re_c \approx 133$ for the $Re_c \approx 147$ for the $\mathcal{R} = 5$ ellipsoid, to be compared with $Re_c \approx 167$ and $Re_c \approx 1360$, respectively. More generally, the new proposed Reynolds number provides a simple and effective global criterion for the prediction of the instability onset: considering a variation in Re_c of one standard deviation around its mean value (both computed with all the cases considered in this study and with weights such that each of the four geometries contributes equally), we obtain 125 ± 20 and can therefore conclude that the flow is likely to be stable when $Re \lesssim 105$ and likely to be unstable when $Re \gtrsim 145$. For comparison, the original critical Reynolds number has a much larger relative spread, $Re_c = 480 \pm 340$.

It is worth noting that the new scaling works well also when other vorticity-related quantities are used instead of $\widetilde{\omega}_{\theta}$, provided that they are a measure of the vorticity generated at the body surface. As an example, in figure 18(b), we keep r_0 as the length scale and use $\widehat{\omega}_{\theta} = U_{rev}/r_0$ as a vorticity scale, which may indeed be seen as a rough estimate of $\widetilde{\omega}_{\theta}$. Again, at criticality, the new proposed Reynolds number $\overline{Re}_c = \widehat{\omega}_{\theta} r_0^2/\nu = U_{rev}r_0/\nu$ collapses rather well for all the considered aspect ratios and geometries to 34 ± 6 . The relevance of U_{rev} on the physics of the instability agrees with the map of the sensitivity to base-flow modifications shown in figures 8 and 9.

6. Conclusion

In this study, we have investigated the primary symmetry-breaking bifurcation of the flow past axisymmetric bodies with a no-slip surface. We have computed the neutral curves $Re_c(\mathcal{R})$ and investigated the instability mechanism using various quantities: structural sensitivity, sensitivity to a base-flow modification or to an increase in Re, dynamics of the perturbation kinetic energy, and endogeneity. We have also proposed a new scaling that is suitable for predicting the onset of the bifurcation. The generality of our conclusions has

been assessed by considering bodies with different geometries (ellipsoids, bullets, cones and bicones) and different aspect ratios ($1 \le R \le 8$).

The instability is driven by the azimuthal vorticity generated at the body surface. We have shown that the mechanism proposed by MM in the context of free-slip spheroidal bubbles well describes the onset of the instability for bodies with a no-slip surface too. In both cases, indeed, the instability arises in a thin region in the near wake, and its onset is strongly related to the occurrence of points where $\partial \omega_{\theta}/\partial r = 0$, i.e. points where isocontours of ω_{θ} align with the radial direction and are perpendicular to the symmetry axis. At these points, the streamwise vorticity gradient $\partial \omega_{\theta}/\partial z$ largely increases with the Reynolds number, favouring the instability.

Having characterised the physical mechanism, we have then proposed a new scaling for the prediction of the instability, in the spirit of the study of Chiarini *et al.* (2022) in the context of 2-D bluff bodies. The new scaling is based on measures of the near-wake azimuthal vorticity, $\widetilde{\omega}_{\theta}$, and the radial extent of the wake recirculation region, r_0 . When computed at criticality, the ensuing Reynolds number $\widehat{Re} = \widetilde{\omega}_{\theta} r_0^2 / \nu$ has been shown to collapse approximately to the same value across all geometries and aspect ratios. This observation can be used to readily estimate whether the steady base flow past axisymmetric bodies is unstable, avoiding a computationally expensive stability analysis, and relying only on an inspection of the base flow.

While the present study focuses on the first instability, it is worth concluding with a word about turbulent wakes. In the turbulent regime, while the mean (time-averaged) flow past an axisymmetric bluff body is itself axisymmetric, the most probable instantaneous flow state is a static m = 1 symmetry-breaking deflection (Grandemange, Gohlke & Cadot 2014; Rigas et al. 2014). The wake visits different azimuthal orientations θ through sudden switches that are triggered by turbulent fluctuations, and that are both random and rare events: the residence time Δt between successive switches follows an exponentially decreasing distribution with no preferred frequency, and the mean residence time $\langle \Delta t \rangle$ is orders of magnitude larger than the convective time L/U_{∞} . Qualitatively similar dynamics is observed in non-axisymmetric bodies with a planar symmetry, such as the Ahmed body (Grandemange, Gohlke & Cadot 2013; Barros et al. 2017). For both types of bluff bodies, static symmetry-breaking deflections of the wake are reminiscent of the primary, laminar pitchfork bifurcation. The understanding of the mechanism of the low-Re instabilities may thus play an important role for the understanding of the flow physics at larger Re and, for example, to locate the most sensitive regions in order to develop new flow control strategies. While the notion of critical Reynolds number may not be relevant in the turbulent regime, it would be interesting to analyse mean turbulent wakes through the lens of the present study. For example, one could evaluate the newly defined Reynolds numbers Re and Re, and investigate how they depend on the geometry, aspect ratio and Re. It may also be worth determining whether regions with $\partial \omega_{\theta}/\partial r < 0$ can be sustained, or if the competition between the production and advection of vorticity is such that $\partial \omega_{\theta}/\partial r > 0$ everywhere in the near wake.

Funding. This research received no specific grant from any funding agency, commercial or not-for-profit sectors.

Declaration of interests. The authors report no conflict of interest.

Appendix A. Characteristic base-flow quantities at Re_c

In § 5, we introduced two new Reynolds numbers, i.e. $\widehat{Re} = \widetilde{\omega}_{\theta} r_0^2 / \nu$ and $\overline{Re} = \widehat{\omega}_{\theta} r_0^2 / \nu = U_{rev} r_0 / \nu$. Figure 19 shows the base-flow quantities involved in the definitions of

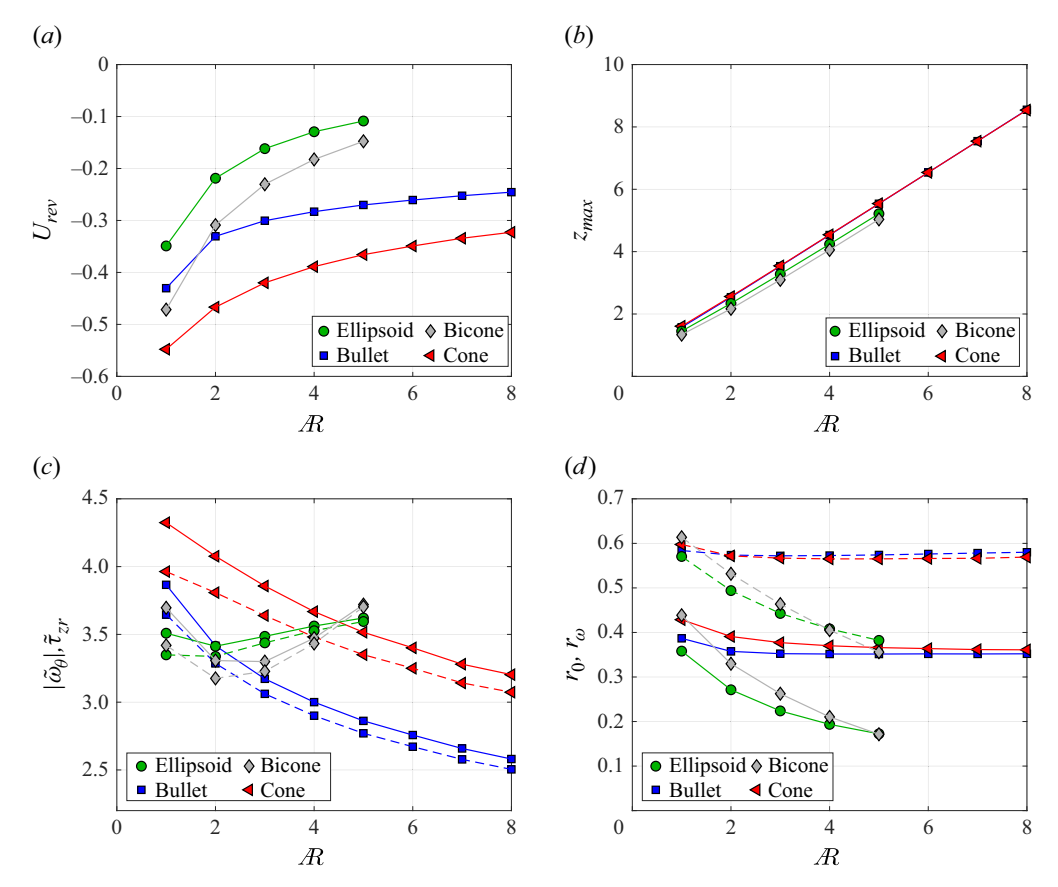


Figure 19. Base-flow quantities at the critical Reynolds number Re_c . (a) Maximum reverse flow U_{rev} . (b) Streamwise location z_{max} of maximum reverse flow. (c) Maximum azimuthal vorticity $\widetilde{\omega}_{\theta}$ (solid lines) and maximum shear $\widetilde{\tau}_{zr}$ (dashed lines) at $z=z_{max}$. (d) Radius r_0 of zero streamwise velocity (solid lines) and radius r_{ω} of maximum azimuthal vorticity (dashed lines) at $z=z_{max}$.

 \widehat{Re} and \overline{Re} , and measured at $Re = Re_c$. They are the maximum reverse flow U_{rev} (figure 19a), the streamwise location z_{max} of maximum reverse flow (figure 19b), the maximum azimuthal vorticity $\widetilde{\omega}_{\theta}$ (and, for reference, the maximum shear $\widetilde{\tau}_{zr}$) at $z = z_{max}$ (figure 19c), and the radius r_0 of zero streamwise velocity (and, for reference, the radius r_{ω} of maximum azimuthal vorticity) at $z = z_{max}$ (figure 19d). We note in particular that for bodies with a zero-thickness TE, $\widetilde{\omega}_{\theta}$ increases with $R \geq 2$, and r_0 decreases, while for bodies with a blunt TE, $\widetilde{\omega}_{\theta}$ decreases and r_0 remains approximately constant.

Appendix B. Mesh convergence

Table 2 reports the critical Reynolds numbers obtained on three different numerical meshes, for all the geometries considered in the present study and for R=1 and 4. From one mesh to the next, all mesh sizes are divided by $\sqrt{2}$, such that the number of elements N_{elmts} increases by a factor of approximately 2. Additionally, table 3 reports the base-flow quantities involved in the definition of the newly introduced Reynolds numbers Re and Re. For illustration purposes, we arbitrarily chose the flow past the Re=1 cone at Re=160. In the present study, we used mesh M2, for which all results are very well converged.

		$\mathcal{R}=1$		$\mathcal{R} = 4$		
Geometry	Mesh	N_{elmts}	Re_c	N_{elmts}	Re_c	
	M1	42 141	212.67	60 643	999.64	
Ellipsoid	M2	79 198	212.67	113 796	999.66	
	M3	150 697	212.66	217 854	999.66	
	M1	44 697	135.13	70 250	758.94	
Bicone	M2	82 757	135.13	129 564	759.02	
	M3	156 943	135.13	244 945	758.90	
	M1	40 207	216.13	51 755	383.87	
Bullet	M2	73 940	216.13	93 773	383.87	
	M3	139 788	216.14	174 449	383.88	
	M1	41 976	164.69	58 107	262.74	
Cone	M2	77 044	164.69	104 849	262.75	
	M3	145 009	164.69	194 017	262.74	

Table 2. Values of the critical Reynolds numbers obtained on three different meshes M1–M3 for the four different geometries, and two aspect ratios each.

Mesh	N_{elmts}	U_{rev}	z_{max}	$\widetilde{\omega}_{ heta}$	$\widetilde{ au}_{zr}$	r_0	r_{ω}
M1	41 976	-0.5737	1.5985	-4.2795	3.9234	0.4255	0.5936
M2	77 044	-0.5737	1.5985	-4.2796	3.9235	0.4255	0.5937
M3	145 009	-0.5737	1.5985	-4.2795	3.9235	0.4255	0.5937

Table 3. Values of the base-flow quantities of figure 19 obtained on three different meshes M1–M3 for the R = 1 cone at Re = 160.

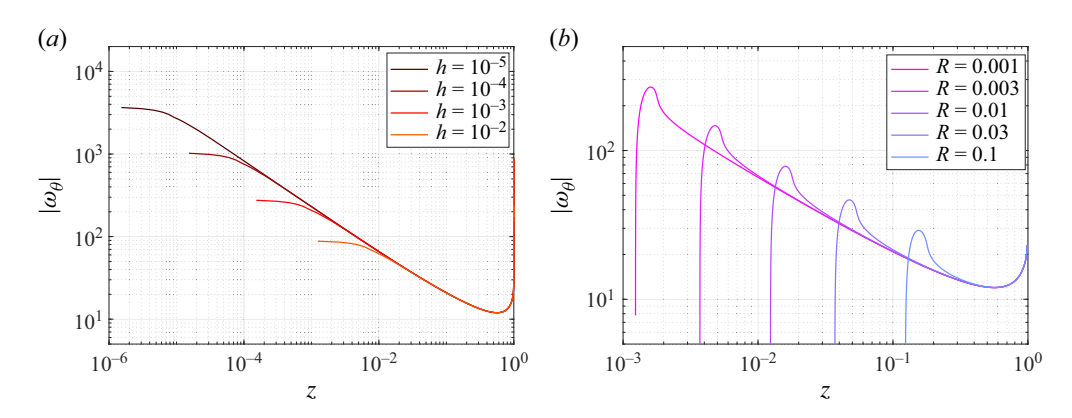


Figure 20. Azimuthal vorticity $\omega_{\theta}(z)$ on the lateral surface of a cone for R=1 at Re=160. (a) Sharp leading edge, varying local mesh size h. (b) Rounded leading edge, varying fillet radius R.

Appendix C. Rounding sharp leading edges

In § 4.1, we reported the maximum vorticity at the wall for ellipsoids and bullets, i.e. bodies with a smooth leading edge. Here, we give more details about bodies with a sharp leading edge.

Figure 20(a) shows the azimuthal vorticity $\omega_{\theta}(z)$ obtained numerically on the surface of an R = 1 cone with a sharp leading edge, at Re = 160. Different curves correspond to

different values of the local mesh size h at the leading edge. The vorticity computed at the sharp leading edge keeps increasing when the numerical mesh is refined locally.

Next, we investigate the effect of smoothing the leading edge with a fillet of radius R. We use a local mesh size h=R/10, and verify convergence with h=R/30. Figure 20(b) shows that the maximum vorticity is obtained slightly downstream of the fillet, and increases as R decreases. However, the critical Reynolds number remains essentially constant (not shown), which is consistent with all the curves $\omega_{\theta}(z)$ collapsing downstream enough (for $z \gtrsim 0.4$ in the present case). Therefore, Re_c and the maximum vorticity are not related.

REFERENCES

- BARROS, D., BORÉE, J., CADOT, O., SPOHN, A. & NOACK, B.R. 2017 Forcing symmetry exchanges and flow reversal in turbulent wakes. *J. Fluid Mech.* 829, R1.
- BATCHELOR, G.K. 1967 An Introduction to Fluid Dynamics, Cambridge University Press.
- BOHORQUEZ, P., SANMIGUEL-ROJAS, E., SEVILLA, A., JIMÉNEZ-GONZÁLEZ, J.I. & MARTÍNEZ-BAZÁN, C. 2011 Stability and dynamics of the laminar wake past a slender blunt-based axisymmetric body. *J. Fluid Mech.* 676, 110–144.
- BRUCKER, C. 2001 Spatio-temporal recontruction of vortex dynamics in axisymmetric wakes. *J. Fluids Struct.* **15** (3–4), 543–554.
- BRØNS, M., THOMPSON, M.C., LEWEKE, T. & HOURIGAN, K. 2014 Vorticity generation and conservation for two-dimensional interfaces and boundaries. J. Fluid Mech. 758, 63–93.
- CHIARINI, A. & BOUJO, E. 2025 Stability and dynamics of the laminar flow past rectangular prisms. J. Fluid Mech. 1008, A33.
- CHIARINI, A., QUADRIO, M. & AUTERI, F. 2021 Linear stability of the steady flow past rectangular cylinders. J. Fluid Mech. 929, A36.
- CHIARINI, A., QUADRIO, M. & AUTERI, F. 2022 A new scaling for the steady flow past two-dimensional bluff bodies. *J. Fluid Mech.* 936, R2.
- CHOMAZ, J.-M. 2005 Global instabilities in spatially developing flows: non-normality and nonlinearity. *Annu. Rev. Fluid Mech.* **37** (1), 357–392.
- CHRUST, M., BOUCHET, G. & DUSEK, J. 2010 Parametric study of the transition in the wake of oblate spheroids and flat cylinders. *J. Fluid Mech.* 665, 199–208.
- COMSOL 1998 Introduction to Comsol Multiphysics[®]. Burlington, MA: COMSOL Multiphysics.
- FABRE, D., AUGUSTE, F. & MAGNAUDET, J. 2008 Bifurcations and symmetry breaking in the wake of axisymmetric bodies. *Phys. Fluids* **20** (5), 051702.
- FORNBERG, B. 1988 Steady viscous flow past a sphere at high Reynolds numbers. *J. Fluid Mech.* **190**, 471–489.
- GIANNETTI, F. & LUCHINI, P. 2007 Structural sensitivity of the first instability of the cylinder wake. *J. Fluid Mech.* **581**, 167–197.
- GRANDEMANGE, M., GOHLKE, M. & CADOT, O. 2013 Turbulent wake past a three-dimensional blunt body. Part 1. Global modes and bi-stability. *J. Fluid Mech.* **722**, 51–84.
- Grandemange, M., Gohlke, M. & Cadot, O. 2014 Statistical axisymmetry of the turbulent sphere wake. *Exp. Fluids* **55** (11), 1–11.
- HAMMOND, D.A. & REDEKOPP, L.G. 1997 Global dynamics of symmetric and asymmetric wakes. J. Fluid Mech. 331, 231–260.
- HILL, M.J.M. 1894 On a spherical vortex. Phil. Trans. R. Soc. 185, 213-245.
- JOHNSON, T.A. & PATEL, V.C. 1999 Flow past a sphere up to a Reynolds number of 300. *J. Fluid Mech.* 378, 19–70.
- LANZERSTORFER, D. & KUHLMANN, H.C. 2012 Global stability of the two-dimensional flow over a backward-facing step. *J. Fluid Mech.* **693**, 1–27.
- LEAL, L.G. 1989 Vorticity transport and wake structure for bluff bodies at finite Reynolds number. *Phys. Fluids A: Fluid Dyn.* 1 (1), 124–131.
- LEGENDRE, D., LAUGA, E. & MAGNAUDET, J. 2009 Influence of slip on the dynamics of two-dimensional wakes. *J. Fluid Mech.* **633**, 437–447.
- LIGHTHILL, M.J. 1963 Introduction: Boundary Layer Theory. Oxford University Press.
- LUNDGREN, T. & KOUMOUTSAKOS, P. 1999 On the generation of vorticity at a free surface. *J. Fluid Mech.* **382**, 351–366.

- MAGARVEY, R.H. & BISHOP, R.L. 1961a Transition ranges for three-dimensional wakes. J. Phys. 39 (10), 1418–1422.
- MAGARVEY, R.H. & BISHOP, R.L. 1961b Wakes in liquid-liquid systems. Phys. Fluids 4 (7), 800-805.
- MAGARVEY, R.H. & MACLATCHY, C.S. 1965 Vortices in sphere wakes. Can. J. Phys. 43 (9), . 1649–1656.
- MAGNAUDET, J. & MOUGIN, G. 2007 Wake instability of a fixed spheroidal bubble. J. Fluid Mech. 572, 311–337.
- MARQUET, O. & LESSHAFFT, L. 2015 Identifying the active flow regions that drive linear and nonlinear instabilities, arXiv:1508.07620.
- MARQUET, O., SIPP, D. & JACQUIN, L. 2008 Sensitivity analysis and passive control of cylinder flow. J. Fluid Mech. 615, 221–252.
- MELIGA, P., CHOMAZ, J.-M. & SIPP, D. 2009a Global mode interaction and pattern selection in the wake of a disk: a weakly nonlinear expansion. *J. Fluid Mech.* **633**, 159–189.
- MELIGA, P., CHOMAZ, J.-M. & SIPP, D. 2009b Unsteadiness in the wake of disks and spheres: instability, receptivity and control using direct and adjoint global stability analyses. J. Fluids Struct. 25 (4), 601–616.
- MELIGA, P., SIPP, D. & CHOMAZ, J.-M. 2010 Open-loop control of compressible afterbody flows using adjoint methods. *Phys. Fluids* 22 (5), 054109.
- MONKEWITZ, P.A. 1988 The absolute and convective nature of instability in two-dimensional wakes at low Reynolds numbers. *Phys. Fluids* **31** (5), 999–1006.
- MONKEWITZ, P.A., HUERRE, P. & CHOMAZ, J.-M. 1993 Global linear stability analysis of weakly non-parallel shear flows. *J. Fluid Mech.* **251**, 1–20.
- MOORE, D.W. 1963 The boundary layer on a spherical gas bubble. J. Fluid Mech. 16 (2), 161-176.
- MORTON, B.R. 1984 The generation and decay of vorticity. *Geophys. Astrophys. Fluid Dyn.* **28** (3–4), 277–308.
- NATARAJAN, R. & ACRIVOS, A. 1993 The instability of the steady flow past spheres and disks. *J. Fluid Mech.* **254**, 323–344.
- PIER, B. 2008 Local and global instabilities in the wake of a sphere. J. Fluid Mech. 603, 39–61.
- RIGAS, G., OXLADE, A.R., MORGANS, A.S. & MORRISON, J.F. 2014 Low-dimensional dynamics of a turbulent axisymmetric wake. J. Fluid Mech. 755, R5.
- SIPP, D., LEBEDEV, A. 2007 Global stability of base and mean flows: A general approach and its applications to cylinder and open cavity flows. *J Fluid Mech* **593**, 333–358.
- TERRINGTON, S.J., HOURIGAN, K. & THOMPSON, M.C. 2020 The generation and conservation of vorticity: deforming interfaces and boundaries in two-dimensional flows. *J. Fluid Mech.* **890**, A5.
- THEOFILIS, V. 2003 Advances in global linear instability analysis of nonparallel and three-dimensional flows. *Prog. Aerosp. Sci.* **39** (4), 249–315.
- THEOFILIS, V. 2011 Global linear instability. Annu. Rev. Fluid Mech. 43 (1), 319–352.
- TOMBOULIDES, A.G. & ORSZAG, S.A. 2000 Numerical investigation of transitional and weak turbulent flow past a sphere. *J. Fluid Mech.* 416, 45–73.
- TRUESDELL, C. 1954 The Kinematics of Vorticity. Indiana University Press.
- Wu, J.-Z. 1995 A theory of three-dimensional interfacial vorticity dynamics. *Phys. Fluids* 7 (10), 2375–2395.
 Wu, J.-Z. & Wu, J.-M. 1993 Interactions between a solid surface and a viscous compressible flow field. *J. Fluid Mech.* 254, 183–211.
- ZAMPOGNA, G.A. & BOUJO, E. 2023 From thin plates to Ahmed bodies: linear and weakly nonlinear stability of rectangular prisms. *J. Fluid Mech.* **966**, A19.